J. Fluid Mech. (2023), *vol*. 955, A39, doi:10.1017/jfm.2022.1080

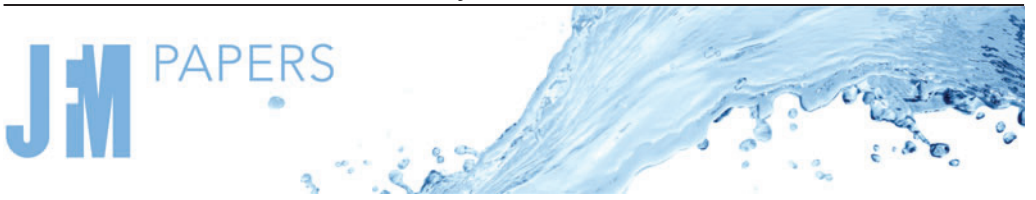

Identification of the energy contributions associated with wall-attached eddies and very-large-scale motions in the near-neutral atmospheric surface layer through wind LiDAR measurements

Matteo Puccioni[1], Marc Calaf[2], Eric R. Pardyjak[2], Sebastian Hoch[2], Travis J. Morrison[2], Alexei Perelet[2] and Giacomo Valerio Iungo[1],†

[1]Wind Fluids and Experiments (WindFluX) Laboratory, Mechanical Engineering Department, The University of Texas at Dallas, 800 W Campbell Rd, 75080 Richardson, TX, USA

[2]Department of Mechanical Engineering, University of Utah, Salt Lake City, UT 84112, USA

(Received 14 August 2022; revised 18 November 2022; accepted 12 December 2022)

Recent works on wall-bounded flows have corroborated the coexistence of wall-attached eddies, whose statistical features are predicted through Townsend's attached-eddy hypothesis (AEH), and very-large-scale motions (VLSMs). Furthermore, it has been shown that the presence of wall-attached eddies within the logarithmic layer is linked to the appearance of an inverse-power-law region in the streamwise velocity energy spectra, upon significant separation between outer and viscous scales. In this work, a near-neutral atmospheric surface layer is probed with wind light detection and ranging to investigate the contributions to the streamwise velocity energy associated with wall-attached eddies and VLSMs for a very-high-Reynolds-number boundary layer. Energy and linear coherence spectra (LCS) of the streamwise velocity are interrogated to identify the spectral boundaries associated with eddies of different typologies. Inspired by the AEH, an analytical model for the LCS associated with wall-attached eddies is formulated. The experimental results show that the identification of the wall-attached-eddy energy contribution through the analysis of the energy spectra leads to an underestimate of the associated spectral range, maximum height attained and turbulence intensity. This feature is due to the overlap of the energy associated with VLSMs obscuring the inverse-power-law region. The LCS analysis estimates wall-attached eddies with a streamwise/wall-normal ratio of about 14.3 attaining a height of about 30 % of the outer scale of turbulence.

† Email address for correspondence: valerio.iungo@utdallas.edu

Key words: boundary layer structure, atmospheric flows, turbulent boundary layers

1. Introduction

Characterizing the organization and energy content of coherent structures present in wall-bounded turbulent flows is important for many engineering and environmental pursuits, such as wind energy (Önder & Meyers 2018), environmental pollutant transport (Reche *et al.* 2018) and urban flows (Barlow 2014). Coherent structures cover a breadth of spatial and temporal scales, including streamwise-aligned packets of hairpin vortices resulting from auto-generation processes, while concatenation processes in the streamwise direction can lead to the generation of structures with a wavelength of the order of 2–3 times the outer scale of turbulence, Δ_E (e.g. the boundary layer thickness), which are denoted as large-scale motions (LSMs) (Adrian 2007; Marusic *et al.* 2010; Smits, McKeon & Marusic 2011; Jiménez 2018). Even larger structures have been detected with streamwise extent in the range of 8-20 Δ_E, denoted as very-large-scale motions (VLSMs) (Kim & Adrian 1999; Hutchins & Marusic 2007), for which a consensus on their generation process has not been achieved yet (Guala, Hommema & Adrian 2006; Balakumar & Adrian 2007). Very-large-scale motions interact with the near-wall turbulence cycle through nonlinear modulation mechanisms (Mathis, Hutchins & Marusic 2009; Talluru *et al.* 2014; Lee & Moser 2019; Liu, Wang & Zheng 2019; Salesky & Anderson 2020).

A cornerstone to achieving an in-depth understanding of the stochastic contribution of coherent structures to the turbulent kinetic energy in wall-bounded flows is the Townsend's attached-eddy hypothesis (AEH) (Townsend 1976), which models the logarithmic layer as a forest of randomly repeated geometrically similar eddies, whose vertical extent, δ, is proportional to their distance from the wall, z, and whose eddy population density is inversely proportional to their size. Furthermore, the geometric similarity of wall-attached turbulent motions and the overlapping between inner scaling with z and outer scaling with Δ_E justify the presence of the k_x^{-1} region (where k_x is the streamwise wavenumber) in the streamwise velocity energy spectrum, ϕ_{uu} (Perry, Henbest & Chong 1986). This spectral feature was also predicted through dimensional analysis (Perry & Abell 1975; Perry *et al.* 1986; Davidson & Krogstad 2009). The spectral extension of this inverse-power-law region is expected to grow with scale separation, and, thus, the friction Reynolds number $Re_\tau = U_\tau \Delta_E/\nu$, where U_τ is the friction velocity ($U_\tau = \sqrt{\tau_0/\rho}$, with τ_0 and ρ being the wall-shear stress and the fluid density, respectively), and ν the kinematic viscosity. However, evidence of the k_x^{-1} spectral region is still elusive even for high Re_τ laboratory data (Morrison *et al.* 2002; Rosenberg *et al.* 2013; Vallikivi, Ganapathisubramani & Smits 2015; Baidya *et al.* 2017), and field observations of the atmospheric surface layer (ASL) (Högström, Hunt & Smedman 2002; Calaf *et al.* 2013).

Perry & Abell (1977), Perry *et al.* (1986), Marusic & Perry (1995) and Perry & Marusic (1995) argued that the coherent structures in wall-bounded flows do not consist of only wall-attached eddies, rather they encompass eddies of different nature. In this scenario, Perry & Marusic (1995) reasoned that three different eddy types exist in a wall-bounded flow: wall-attached eddies described by the AEH (type $\mathcal{A}$ eddies), wall-detached eddies (type $\mathcal{B}$ eddies), referring to large-scale structures, superstructures and VLSMs (Högström 1990, 1992; Högström *et al.* 2002; Baars & Marusic 2020*a*; Hu, Yang & Zheng 2020), and Kolmogorov small-scale eddies (type $\mathcal{C}$), which dominate the $k_x^{-5/3}$ inertial subrange of the streamwise velocity energy spectrum. Despite the capability of the AEH in providing an accurate representation of the stochastic energetic contribution of wall-attached eddies

to the logarithmic layer of wall-bounded turbulent flows, the stochastic identification of turbulent coherent structures of different nature, i.e. type $\mathcal{A}$, $\mathcal{B}$ or $\mathcal{C}$ eddies according to the classification proposed by Perry & Marusic (1995), is still elusive.

A common technique used to separate the energetic contributions due to coherent structures and, specifically, to isolate the energy connected with wall-attached eddies, is to apply a band-pass filter to the streamwise velocity signals (e.g. Nickels *et al.* 2005; Hwang 2015; Hu *et al.* 2020). The AEH assumes that wall-attached eddies scale as their wall-normal distance, and, thus, the high-wavenumber limit of a band-pass filter aiming at isolating the wall-attached-eddy contribution from the streamwise velocity spectrum should be proportional to z (Perry & Chong 1982; Meneveau & Marusic 2013; Yang & Meneveau 2019; Baars & Marusic 2020*a*; Hu *et al.* 2020). Furthermore, the streamwise velocity within the logarithmic layer at a given wall-normal position results from the superposition of contributions induced by wall-attached eddies within the vertical range between z and Δ_E. Therefore, the low-frequency limit of a potential band-pass filter should scale with the boundary layer thickness, Δ_E (Baars & Marusic 2020*a*; Hu *et al.* 2020). While there is consensus on the filtering approach to isolate the energetic contribution associated with wall-attached eddies, on the other hand, there are broad discrepancies on the actual spectral limits used for this band-pass filter.

Another technique to separate the energy content associated with coherent structures of different nature was proposed in Baars & Marusic (2020*a*). In their study, the authors generated two spectral filters based on the linear coherence spectrum (LCS) obtained from the streamwise velocity signals collected at a given height and two reference positions, one located in the proximity of the wall and another within the logarithmic layer. Using this data-driven approach, the authors found that the coherence-based low-wavelength limit of the k_x^{-1} spectral region was proportional to the wall-normal position ($\lambda_x \geq 14z$, where λ_x is the streamwise wavelength), while the high-wavelength limit was proportional to Δ_E.

As mentioned above, the spectral extension of the inverse-power-law region grows with the separation between the outer scale of turbulence, Δ_E, and the viscous scale, ν/U_τ. This requirement has spurred the development of experimental facilities (Marusic *et al.* 2010; Smits *et al.* 2011; Marusic & Monty 2018) and numerical tools (Jiménez 2004; Jiménez & Moser 2007; Lee & Moser 2015, 2019) enabling investigations of wall-bounded flows at high Reynolds numbers. For the same purpose, the ASL represents a unique opportunity to probe a boundary layer with extremely high Reynolds numbers (Metzger, Mckeon & Holmes 2007; Guala, Metzger & McKeon 2011; Hutchins *et al.* 2012; Liu, Bo & Liang 2017; Heisel *et al.* 2018; Huang *et al.* 2021; Li, Wang & Zheng 2021) upon filtering out velocity fluctuations connected with non-turbulent scales (Larsén, Vincent & Larsén 2013; Larsén, Larsén & Petersen 2016), restricting the data set to subsets presenting negligible effects connected with the atmospheric thermal stratification (Wilson 2008), and strictly verifying the statistical stationarity and convergence of the collected measurements (Metzger *et al.* 2007). Analogies between ASL and laboratory flows have already been investigated for several features of turbulent boundary layers, such as near-wall structures (Klewicki *et al.* 1995), hairpin vortex packets (Hommema & Adrian 2003), Reynolds stresses (Kunkel & Marusic 2006; Marusic *et al.* 2013), inclination angle of coherent structures (Liu *et al.* 2017), uniform momentum zones (Heisel *et al.* 2018), large-scale amplitude modulation process (Liu *et al.* 2019) and LCS (Krug *et al.* 2019; Li *et al.* 2021).

Probing ASL flows requires measurement techniques providing sufficient spatio-temporal resolution throughout the ASL thickness. In this realm, wind light detection and ranging (LiDAR) has become a compelling remote sensing technique to investigate atmospheric turbulence. For instance, LiDAR scans can be optimally designed to probe the atmospheric

boundary layer and wakes generated by utility-scale wind turbines (e.g. El-Asha, Zhan & Iungo 2017; Zhan, Letizia & Iungo 2020; Letizia, Zhan & Iungo 2021*a*,*b*). Regarding atmospheric turbulence, LiDAR measurements were used to detect the inverse-power law (Calaf *et al.* 2013) or the inertial sublayer (Iungo, Wu & Porté-Agel 2013) from the streamwise velocity energy spectra. Multiple simultaneous and co-located LiDAR measurements can be leveraged to measure three-dimensional (3-D) velocity components and Reynolds stresses (Mikkelsen *et al.* 2008; Mann *et al.* 2009; Carbajo Fuertes, Iungo & Porté-Agel 2014). More recently, the LiDAR technology was assessed against sonic anemometry during the experimental planetary boundary layer instrumentation assessment (XPIA) campaign showing excellent agreement in probing the horizontal velocity component (Debnath *et al.* 2017*a*,*b*; Lundquist *et al.* 2017).

In this work, streamwise velocity measurements collected simultaneously at various wall-normal positions throughout the ASL thickness with a pulsed Doppler scanning wind LiDAR and a sonic anemometer are investigated to identify the spectral boundaries and the maximum vertical extent of the energy contributions associated with wall-attached eddies. The velocity data were collected through fixed scans performed with the azimuth angle of the LiDAR scanning head set along the mean wind direction during near-neutral thermal conditions. After the quantification of the spectral gap and estimation of the outer scale of turbulence, Δ_E, the identification of the energy associated with eddies of different nature is performed through two independent methods: first, from the streamwise velocity energy spectra by leveraging the semi-empirical spectral model proposed by Högström *et al.* (2002); then, from the LCS obtained between the LiDAR data collected at a reference height and various wall-normal positions, in analogy with the approach proposed by Baars, Hutchins & Marusic (2017). Finally, the integrated streamwise energy within both the spectral portion associated with wall-attached eddies, and that due to coherent structures with larger wavelengths, e.g. LSMs, VLSMs and superstructures, is evaluated along the wall-normal direction and assessed against previous laboratory studies.

The remainder of the paper is organized as follows. In § 2 the experimental data set is introduced, while the methodology to analyse the streamwise velocity spectrum and LCS is described in § 3. In § 4 the results on the identification of turbulent coherent structures of different nature and the quantification of their energy content are discussed. Finally, concluding remarks are reported in § 5.

In this work a Cartesian reference frame is used, where (x, y, z) represent the streamwise, spanwise and wall-normal directions, respectively. The respective mean velocity vector is indicated as $\boldsymbol{U} = (U, V, W)$, while the zero-mean velocity fluctuations are $\boldsymbol{u} = (u, v, w)$. The overbar denotes the Reynolds average, t is time and the superscript '+' for a dimension of length indicates the viscous scaling with ν/U_τ, while outer scaling is performed via Δ_E.

2. Experimental data set

2.1. *The LiDAR field campaign*

Wind and atmospheric data were collected during the idealized planar array experiment for quantifying surface heterogeneity (IPAQS) campaign performed in June 2018 at the surface layer turbulence and environmental science test (SLTEST) site (Huang *et al.* 2021). This site is located in the south–west part of the dry Great Salt Lake, Utah, within the Dugway Proving Ground military facility. The SLTEST site is characterized by an extremely barren and flat ground (≈1 m elevation difference every 13 km) and exceptionally long unperturbed extensions (≈240 km and ≈48 km in the north–south and east–west directions, respectively) (Kunkel & Marusic 2006). The typical terrain

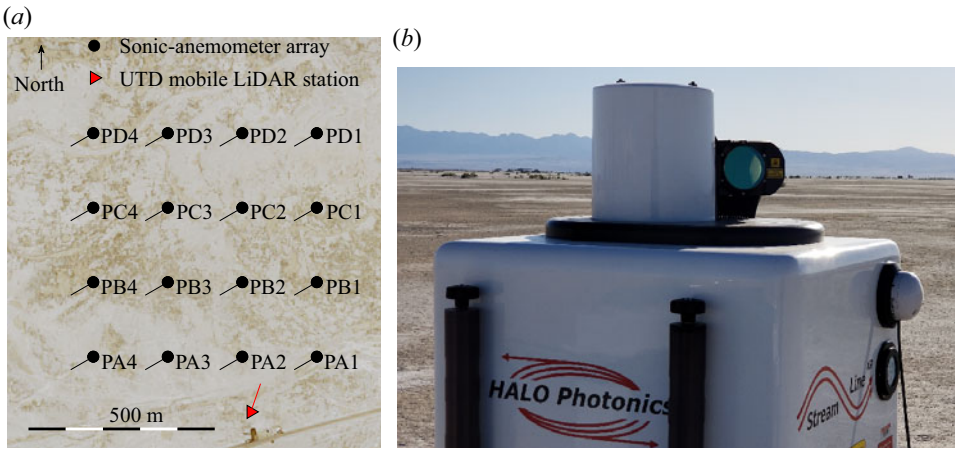

Figure 1. The LiDAR field campaign. (*a*) Aerial view of the instrument locations. Lines represent the orientation of each instrument, while the labels report the names of each sonic anemometer. (*b*) Photo of the scanning Doppler wind LiDAR.

coverage consists of bushes over dry and salty soil, which allow classifying the terrain as transitionally rough (Ligrani & Moffat 1986; Kunkel & Marusic 2006). During the experimental campaign, several instruments were simultaneously deployed for different scientific purposes. The mobile LiDAR station (red triangle in figure 1*a*) of the University of Texas at Dallas was deployed in the proximity of a 4-by-4 array of CSAT3 3-D sonic anemometers (black circles in figure 1*a*), manufactured by Campbell Scientific Inc., which recorded the three velocity components and temperature with a sampling frequency of 20 Hz. The sonic-anemometer data considered for this study were collected from the station indicated as 'PA2' in figure 1(*a*) at a 2 m height. The sonic-anemometer data were firstly corrected for pitch and yaw misalignment following the procedure proposed by Wilczak, Oncley & Stage (2001), then high-pass filtered as per Hu *et al.* (2020) with a cutoff frequency $f_{gap} = 0.0055$ Hz, whose selection is discussed in Appendix A.

To investigate a canonical near-neutral boundary layer, the effects of atmospheric stability on the velocity field should be accounted for. Regarding atmospheric boundary layer flows, the buoyancy contribution to turbulence is compared with the shear-generated turbulence through the Obukhov length, L (Monin & Obukhov 1954),

$$L = -\frac{U_\tau^3 T}{\kappa g \overline{w\theta}}, \tag{2.1}$$

where T is the mean virtual potential temperature (in Kelvin), $\kappa = 0.41$ is the von Kármán constant, $\overline{w\theta}$ is the vertical heat flux and g is the gravity acceleration. Sonic-anemometer data from the PA2 station are further leveraged to calculate the friction velocity according to the eddy-covariance method (Stull 1988),

$$U_\tau = (\overline{uw}^2 + \overline{vw}^2)^{1/4}. \tag{2.2}$$

The pulsed scanning Doppler wind LiDAR deployed for this experiment is a Streamline XR manufactured by Halo Photonics, whose technical specifications are reported in table 1 while a photo of its deployment for the IPAQS field campaign is reported in figure 1(*b*). A Doppler wind LiDAR allows probing the atmospheric wind field utilizing a laser beam whose light is backscattered due to the presence of particulates suspended

Parameter	Value
Wavelength (μm)	1.5
Repetition rate (kHz)	10
Velocity resolution ($m\,s^{-1}$)	±0.0764
Velocity bandwidth ($m\,s^{-1}$)	±38
Number of FFT points	1024
Radial range (m)	45 to 10 000
Azimuth angle (range) (°)	0° to 360°
Elevation angle (range) (°)	−10° to 190°
LiDAR gate length (m)	18
Number of gates	200
Sampling rate (Hz)	1

Table 1. Technical specifications of the scanning Doppler wind LiDAR Streamline XR.

in the atmosphere. The velocity component along the laser-beam direction, denoted as radial velocity, V_r, is evaluated from the Doppler shift of the backscattered laser signal (Sathe & Mann 2013). A pulsed Doppler wind LiDAR emits laser pulses to perform quasi-simultaneous wind measurements at multiple distances from the LiDAR as the pulses travel in the atmosphere. The wind measurements performed over each probe volume, which is referred to as range gate, can be considered as the convolution of the actual wind velocity field projected along the laser-beam direction with a weighting function representing the radial distribution of the energy associated with each laser pulse (Frehlich, Hannon & Henderson 1998). Therefore, the radial velocity, V_r, can be expressed in terms of the instantaneous wind velocity components, $(U(t), V(t), W(t))$, where the x direction is considered aligned with the mean wind direction, Θ_w, as

$$V_r(t) = U(t)\cos\Theta\cos\Phi + V(t)\sin\Theta\cos\Phi + W(t)\sin\Phi, \tag{2.3}$$

where Θ is the LiDAR azimuth angle and Φ is the elevation angle. Both of these angles are measured with a digital inclinometer with an accuracy of 0.005° embedded in the LiDAR.

To maximize the spatio-temporal resolution of the LiDAR measurements and accuracy in probing the streamwise velocity component, fixed LiDAR scans were performed with a low elevation angle ($\Phi = 3.5°$) and with the laser beam aligned with the mean wind direction, which is monitored by the PA2 sonic anemometer, namely with $V \approx 0$ (Iungo *et al.* 2013). During the post-processing, only LiDAR data sets with an instantaneous deviation of the wind direction smaller than ±10° from the respective 10 minute average have been considered (Hutchins *et al.* 2012). Considering the low elevation angle used and the azimuth angle aligned with the mean wind direction, the first-order approximation for the mean streamwise velocity measured through the wind LiDAR is obtained from (2.3) as $U \approx V_r/\cos\Phi$, while for the variance is $\overline{uu} \approx \overline{v_r v_r}/\cos^2\Phi$ (Zhan *et al.* 2020).

As previously mentioned, the LiDAR radial velocity is measured through a convolution of the LiDAR laser pulse with the actual velocity field over each range gate. This spatial averaging leads to an underestimation of the measured streamwise turbulence intensity. In this work the streamwise velocity energy spectra, and the respective turbulence intensity obtained as an integral over the measured spectral range, are corrected for the spatial averaging associated with the LiDAR measuring process by using the methodology proposed in Puccioni & Iungo (2021). For the present set-up, the applied spectral correction only affects the inertial subrange of the streamwise velocity energy spectra

calculated for heights larger than the LiDAR range gate (18 m). The reader can refer to Appendix B for more details.

Based on the data quality control described in the following subsection, a subset of one hour of LiDAR data collected during the day of 10 June 2018, from 09:00 AM to 10:00 AM UTC (local time −6 hours) is selected for further analyses, which is characterized by a friction velocity of $U_\tau = 0.42\,\mathrm{m\,s^{-1}}$, Obukhov length of $L = -278\,\mathrm{m}$, which corresponds to a stability parameter of $z/L = -0.007$ indicating a near-neutral atmospheric stability regime (Högström *et al.* 2002; Kunkel & Marusic 2006; Metzger *et al.* 2007; Mouri, Morinaga & Haginoya 2019; Huang *et al.* 2021). For the selected data set, the kinematic viscosity has been estimated $\nu = 1.49 \times 10^{-5}\,\mathrm{m^2\,s^{-1}}$ based on the mean temperature of 290 K recorded by the sonic anemometer (Picard *et al.* 2008).

2.2. *Quality control of the LiDAR data*

The LiDAR measurements undergo a quality control procedure to ensure the reliability and accuracy of the velocity data. The first parameter used to ensure the accuracy of the LiDAR velocity measurements is the carrier-to-noise ratio (CNR), which represents a quantification of the intensity of the backscattered laser pulse over the typical signal noise as a function of the radial distance and time (Frehlich 1997; Beck & Kühn 2017; Gryning & Floors 2019). For a fixed scan with a constant elevation angle, the range gates selected for any further analysis have a time-averaged CNR not lower than −20 dB (Gryning & Floors 2019), which corresponds for the selected data set to all the LiDAR measurements collected within the vertical range between 6 and 143 m with a vertical resolution of approximately 1.08 m. Considering an elevation angle of the laser beam of 3.5°, the horizontal range between the first and last LiDAR range gate is then 2246 m.

A filtering procedure is then adopted to remove possible outliers from the LiDAR data, i.e. erroneous estimation of the radial velocity from the backscattered LiDAR signal (Frehlich *et al.* 1998). In this study a standard deviation-based filter is implemented, i.e. any velocity sample out of the interval $U \pm 3.5\overline{uu}^{1/2}$, which is estimated for the entire 1 h period of the selected data set, is marked as an outlier and removed (Højstrup 1993; Vickers & Mahrt 1997). The rejected samples are then replaced through a bi-harmonic algorithm with the Matlab function *inpaint_nans* (D'Errico 2004). In the worst scenario, the total number of samples rejected for the data collected at a 140-m height is 0.75 % over the 1 h duration of the selected data set. The LiDAR signal quality typically improves by approaching the LiDAR due to the increased energy in the laser beam.

Subsequently, the statistical stationarity of the velocity signals is analysed through the standard deviation dispersion (SDD), which is calculated as (Foken & Wichura 1996)

$$\mathrm{SDD} = \frac{\sqrt{\langle(\sigma_i - \sigma_0)^2\rangle_i}}{\sigma_0} \times 100, \tag{2.4}$$

where σ_0 is the standard deviation of a velocity signal over its entire sampling period of 1 h, and σ_i is the velocity standard deviation calculated over a subset with a 5 min duration. The symbol $\langle\rangle_i$ indicates the average over the total number of non-overlapping subsets of the original velocity signal. The parameter SDD is plotted in figure 2(*a*) indicating that throughout the vertical range probed by the LiDAR, the statistical stationarity of the velocity signals can be assumed considering a threshold for the SDD parameter of 30 % (Foken *et al.* 2004).

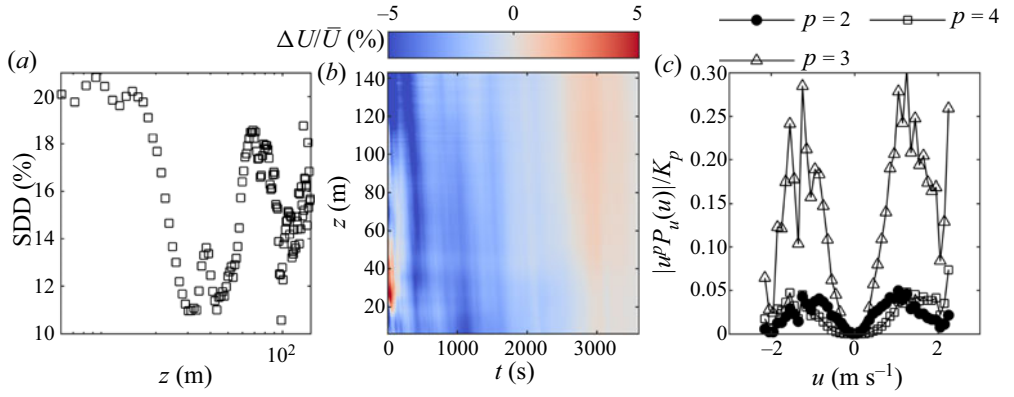

Figure 2. Analysis of the statistical stationarity and convergence of the LiDAR data. (*a*) The SDD parameter as a function of height. (*b*) Percentage difference between cumulative mean for different signal durations, t, and the mean for the entire 1 h duration of the LiDAR velocity data, $\bar{U}$. (*c*) Normalized absolute value of premultiplied probability density functions for the velocity signal collected at $z = 143$ m for statistical moments with a different order, p.

The convergence of the mean velocity is then analysed for an increasing number of samples (Heisel *et al.* 2018). In figure 2(*b*) the results of this analysis show that velocity signals with a duration of at least roughly 3000 s are needed to achieve a statistical convergence of the mean value. Furthermore, the statistical convergence of the mean streamwise velocity is comparable among the different heights probed. Finally, the convergence of higher-order statistical moments is qualitatively investigated by inspecting the probability density function of the velocity signal, $P_u(U)$, for the highest range gate, premultiplied by u^p, where p is the order of the considered central statistical moment. If the tails of the considered function smoothly taper towards zero, then the respective statistical moment, K_p, can be considered as adequately estimated through the available data (Meneveau & Marusic 2013). For the present study, this analysis is performed considering velocity bins with a width of 0.1 m s^{-1}. In figure 2(*c*) the results suggest a good convergence for the second-order statistics and an incomplete convergence for higher-order statistical moments. The latter is not crucial for the following analyses because higher-order statistics, e.g. skewness and kurtosis, will not be involved.

2.3. *Streamwise mean velocity and turbulence intensity*

The mean streamwise velocity measured through the wind LiDAR and the PA2 sonic anemometer is scaled with the friction velocity retrieved from the sonic-anemometer data, then compared in figure 3(*a*) to ASL data collected from previous experiments at different sites with variable terrain roughness (Clarke *et al.* 1971; Kunkel & Marusic 2006; Tieleman 2008; Hutchins *et al.* 2012; Wang & Zheng 2016; Heisel *et al.* 2018), and laboratory experiments as well (Schultz & Flack 2007; Squire *et al.* 2016; Morrill-Winter *et al.* 2017). For an ASL flow, the effects of the terrain roughness on the mean streamwise velocity can be accounted through the aerodynamic roughness length, z_0, into the logarithmic law of the wall (Kunkel & Marusic 2006; Gryning *et al.* 2007;

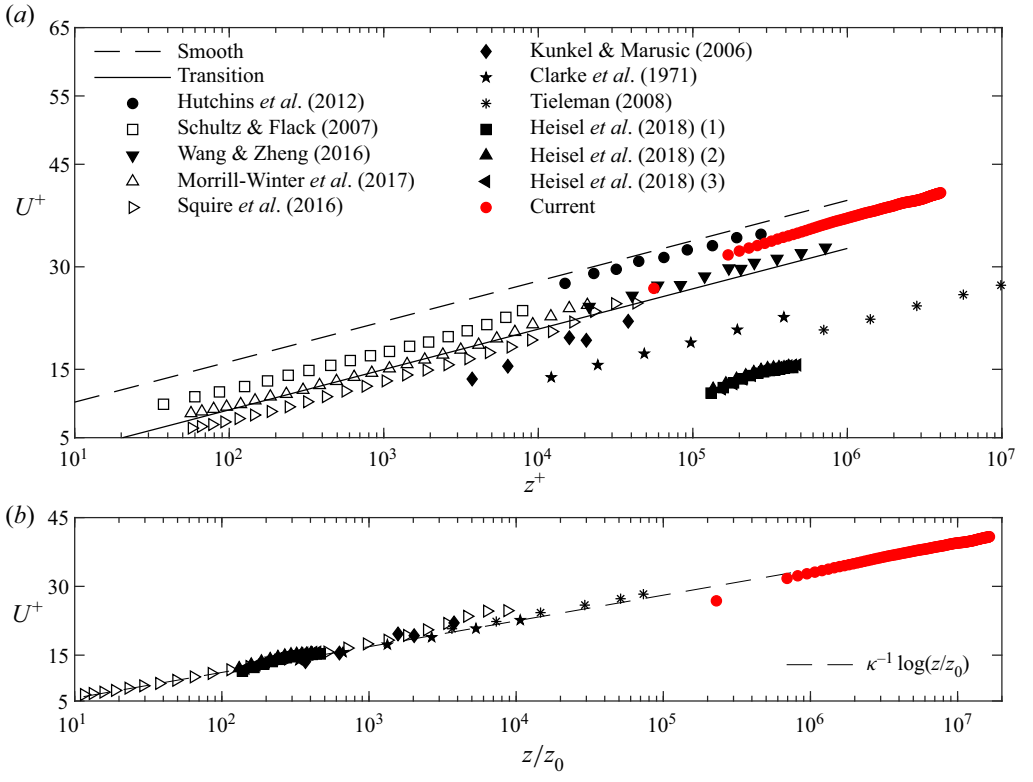

Figure 3. Mean streamwise velocity measured from the LiDAR and the PA2 sonic anemometer (the lowest point). (*a*) Mean velocity versus inner-scaled wall-normal coordinate. (*b*) Wall-normal coordinate is made non-dimensional with the aerodynamic roughness length, z_0. Empty and filled symbols refer to wind tunnel and ASL studies, respectively. This figure is adapted from Heisel *et al.* (2018).

Metzger *et al.* 2007; Heisel *et al.* 2018),

$$U^+ = \frac{1}{\kappa}\left[\log\left(\frac{z}{z_0}\right) - \Psi\left(\frac{z}{L}\right)\right], \tag{2.5}$$

where Ψ is the stability correction function (Businger *et al.* 1971). The experimental data are fitted with (2.5) to estimate the aerodynamic roughness length, which results in $z_0 = 8.71 \times 10^{-6}$ m. By normalizing the wall-normal position with z_0, a very good agreement is observed in figure 3(*b*) between the stability-corrected mean streamwise velocity measured by the LiDAR and previous data sets. Furthermore, (2.5) is used to assess the value of U_τ calibrated on the LiDAR data ($U_\tau = 0.51 \pm 0.009\,\mathrm{m\,s^{-1}}$) against that estimated from the sonic-anemometer data using the eddy-covariance method ($U_\tau = 0.42\,\mathrm{m\,s^{-1}}$).

Another way to account for the terrain roughness on the mean streamwise velocity profile is through the sand-grain roughness parameter, k_s^+,

$$U^+ = \frac{1}{\kappa}\log\left(\frac{z^+}{k_s^+}\right) + B(k_s^+), \tag{2.6}$$

where $B(k_s^+)$ is a function accounting for the vertical shift of the mean velocity profile. For a transitional roughness regime, where $2.25 \leq k_s^+ \leq 90$ (Ligrani & Moffat 1986;

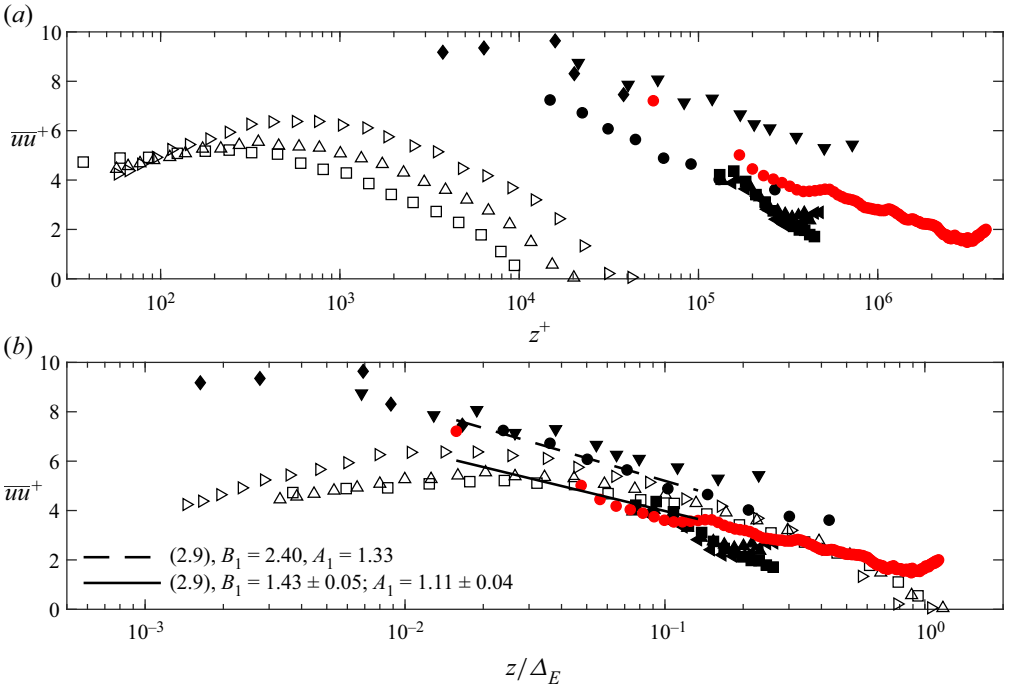

Figure 4. Wall-normal profile of turbulence intensity with the (*a*) inner-scaled and (*b*) outer-scaled wall-normal coordinate. For the current data set, the lowest point is retrieved from the PA2 sonic anemometer. In (*b*) the black continuous line refers to the model of Marusic *et al.* (2013) calibrated on the present data set. Legend as for figure 3. This figure is adapted from Heisel *et al.* (2018).

Hutchins *et al.* 2012), $B(k_s^+)$ is given by (Kunkel & Marusic 2006)

$$B(k_s^+) = \frac{1}{\kappa}\log k_s^+ + 5.0 + \sin\left(\frac{\pi h}{2}\right)\left(8.5 - 5.0 - \frac{1}{\kappa}\log k_s^+\right), \tag{2.7}$$

where

$$h = \frac{\log(k_s^+/90)}{\log(k_s^+/2.25)}. \tag{2.8}$$

Comparing (2.5) and (2.6), the sand-grain roughness can be estimated from z_0 as $k_s^+ = 11.4$ ($k_s = 0.41$ mm), which is of the same order of magnitude as for previous estimates for the SLTEST site, e.g. $k_s^+ \approx 34$ ($k_s = 2.9$ mm) in Kunkel & Marusic (2006), or $k_s^+ = 15$ in Huang *et al.* (2021).

The inner-scaled wall-normal profile of the turbulence intensity is reported against the viscous- and outer-scaled wall-normal coordinate in figure 4(*a*,*b*), respectively. The estimate of the outer scale of turbulence, $\Delta_E = 127$ m for the present data set, is detailed in Appendix A. Based on the AEH, the law for the wall-normal distribution of streamwise turbulence intensity can be written as (Townsend 1976; Perry & Chong 1982)

$$\overline{uu}^+ = B_1 - A_1 \log\left(\frac{z}{\Delta_E}\right), \tag{2.9}$$

where B_1 is a flow-dependent constant accounting for the large-scale inactive motion, while A_1 is the Townsend–Perry constant (Perry *et al.* 1986; Baars & Marusic 2020*b*).

For the SLTEST site under neutral conditions, Marusic *et al.* (2013) reported that $A_1 = 1.33 \pm 0.17$ and $B_1 = 2.14 \pm 0.40$, whereas for the current data set we obtain $A_1 = 1.11 \pm 0.04$ and $B_1 = 1.43 \pm 0.05$.

3. Contribution of eddies with different typology to the streamwise velocity energy

3.1. *Reynolds stresses and isolated-eddy function*

According to the AEH, a wall-attached eddy has a wall-normal extent, δ, growing linearly with the distance from the wall, z (Townsend 1976; Perry & Chong 1982). Therefore, the probability density function representing the occurrence of an eddy with size δ, $p_H(\delta)$, should decrease monotonically with z (Townsend 1976),

$$p_H(\delta) = \begin{cases} \dfrac{M}{\delta} & \text{as } \delta_1 \leq \delta \leq \Delta_E, \\ 0 & \text{otherwise}, \end{cases} \tag{3.1}$$

where M is a constant related to the eddy population density on the plane of the wall (De Silva, Hutchins & Marusic 2015), and $\delta_1 \approx 100\nu/U_\tau$ is the smallest eddy size owning to the logarithmic layer, which is fixed by the viscous cutoff (Kline *et al.* 1967; Perry & Chong 1982). The Reynolds stresses at a given z are then calculated as the weighted integral of isolated-eddy contributions over the entire scale range,

$$\overline{u_i u_j}^+ = \int_{\delta_1}^{\Delta_E} I_{ij}\left(\frac{z}{\delta}\right) p_H(\delta)\,\mathrm{d}\delta = \int_{\delta_1}^{\Delta_E} M I_{ij}\left(\frac{z}{\delta}\right)\frac{\mathrm{d}\delta}{\delta} = \int_{z/\Delta_E}^{z/\delta_1} M I_{ij}\left(\frac{z}{\delta}\right)\frac{\delta}{z}\mathrm{d}\left(\frac{z}{\delta}\right), \tag{3.2}$$

where the function I_{ij} is referred to as the 'eddy function', representing the geometrically self-similar isolated-eddy contribution to $\overline{u_i u_j}^+$. In the view of the AEH, I_{ij} is determined by the sole geometrical features of the archetypal wall-attached eddy. Remarkably, I_{ij} can also be estimated for a fixed eddy size, δ, through the differential form of (3.2),

$$I_{ij}\left(\frac{z}{\delta}\right) = -\frac{z}{M}\frac{\partial \overline{u_i u_j}^+}{\partial z}. \tag{3.3}$$

The term on the right-hand side of (3.3) is commonly referred to as the 'indicator function' and it has been used to detect the presence and extent of the logarithmic region (e.g. Bernardini, Pirozzoli & Orlandi 2014; Lee & Moser 2015; Hwang & Sung 2018; Yamamoto & Tsuji 2018; Klewicki 2021). It is noteworthy that (3.3) represents the contribution to the Reynolds stresses of the sole wall-attached eddies (type $\mathcal{A}$), and, thus, does not encompass the contribution of wall-detached eddies, or coherent structures characterized by larger wavelengths, e.g. VLSMs and superstructures (type $\mathcal{B}$).

3.2. *Regions of the streamwise velocity energy spectrum*

Regarding the streamwise velocity spectrum, as mentioned in § 1, for wall-normal locations owning to the inertial layer, the non-dimensional low-wavenumber limit of the k_x^{-1} region (denoted as F following the notation of Perry *et al.* 1986) scales with Δ_E (Perry & Chong 1982; Perry *et al.* 1986). Therefore, the large eddies with scale $O(\Delta_E)$ will contribute to the streamwise velocity energy spectrum as

$$\phi_{uu}^+(k_x\Delta_E) = g_1(k_x\Delta_E) = \frac{\phi_{uu}(k_x)}{\Delta_E U_\tau^2}. \tag{3.4}$$

On the other hand, the non-dimensional high-wavenumber limit of the inverse-power-law spectral region, P, scales with z, and the respective eddies contribute to the streamwise

velocity energy spectrum as

$$\phi^+_{uu}(k_x z) = g_2(k_x z) = \frac{\phi_{uu}(k_x)}{z U_\tau^2}. \tag{3.5}$$

Considering an overlapping region where (3.4) and (3.5) hold simultaneously, and, thus, equating $\phi_{uu}(k_x)$ from (3.4) and (3.5), we obtain

$$\frac{g_1(k_x \Delta_E)}{g_2(k_x z)} = \frac{z}{\Delta_E}. \tag{3.6}$$

Therefore, within this overlapping region, g_1 and g_2 must be of the form (Perry & Abell 1975; Perry *et al.* 1986; Davidson & Krogstad 2009)

$$g_1(k_x \Delta_E) = \frac{A_1}{k_x \Delta_E}; \quad g_2(k_x z) = \frac{A_1}{k_x z}, \tag{3.7a,b}$$

where A_1 is the Townsend–Perry constant, which is of the order of 1 (Perry *et al.* 1986; Baars & Marusic 2020*b*). The turbulence intensity associated with wall-attached eddies is then expressed as the integral of the streamwise velocity energy spectrum over the different regions, i.e.

$$\overline{uu}^+ = \int_0^F g_1(k_x \Delta_E)\, \mathrm{d}(k_x \Delta_E) + \int_{Fz/\Delta_E}^P g_2(k_x z)\, \mathrm{d}(k_x z) + \int_P^\infty \phi^+_{uu}(k_x z)\, \mathrm{d}(k_x z). \tag{3.8}$$

A similar approach for the identification of different regions of the streamwise velocity energy spectrum was proposed by Högström *et al.* (2002) for ASL flows. Specifically, three different regions are singled out within the turbulence spectral range by this model, which are indicated with dashed lines in the sketch reported in figure 5. Region (i) is the inertial subrange, which follows the Kolmogorov law

$$k_x^+ \phi^+_{uu}(k_x) = \frac{\alpha_K}{(2\pi\kappa)^{2/3}} \varphi_\varepsilon^{2/3} \left(\frac{k_x z}{2\pi}\right)^{-2/3}, \tag{3.9}$$

where α_K is the Kolmogorov constant, κ is the von Kármán constant and φ_ε is the non-dimensional dissipation rate, which can be estimated as follows (Kaimal *et al.* 1972):

$$\varphi_\varepsilon^{2/3}\left(\frac{z}{L}\right) = \left(\frac{\kappa z \varepsilon}{U_\tau^3}\right)^{2/3} = \begin{cases} 1 + 0.5\left|\dfrac{z}{L}\right|^{2/3}, & -2 \le z/L \le 0, \\ 1 + 2.5\left|\dfrac{z}{L}\right|^{3/5}, & 0 \le z/L \le 2. \end{cases} \tag{3.10}$$

Here ε is the turbulent kinetic energy dissipation rate and L is the Obukhov length (see § 2.1). It is noted that the maximum value attained by the stability correction function in (3.10) is equal to 1.32 at $z = 143$ m for the data set under investigation.

Region (ii) corresponds to the spectral range where the premultiplied spectrum is nearly constant,

$$k_x^+ \phi^+_{uu}(k_x) \approx A_1, \tag{3.11}$$

where A_1 is the Townsend–Perry constant in (2.9). The wall-normal range where region (ii) was observed in the ASL, which is dubbed the 'eddy surface layer' (ESL), has a thickness of about $\Delta_E/3$ (Hunt & Morrison 2000; Högström *et al.* 2002). This estimate is similar to that for the height of the logarithmic layer for ASL flows reported in

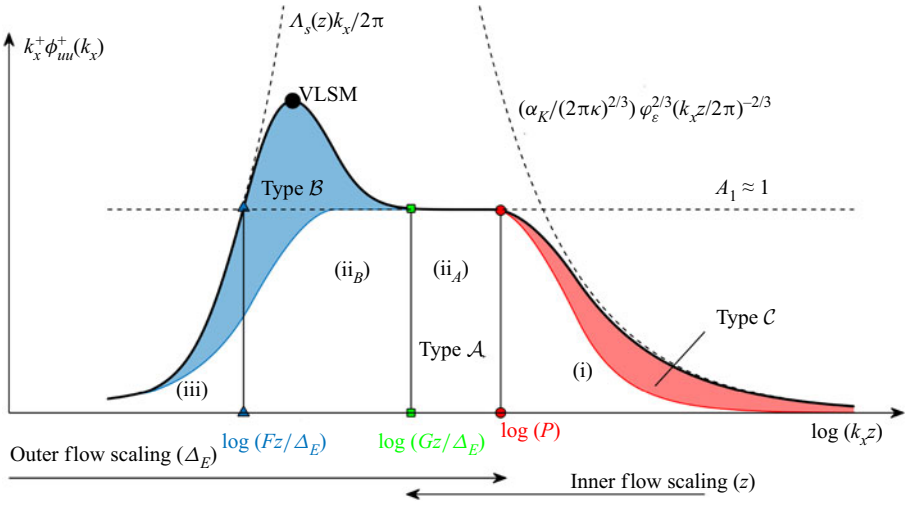

Figure 5. Sketch of the different regions encompassed in the streamwise velocity premultiplied energy spectrum.

Hutchins *et al.* (2012), while Marusic *et al.* (2013) conservatively quantified the height of the logarithmic layer based on mean velocity profiles and turbulence intensity at $z = 0.15\Delta_E$ for laboratory flows.

For region (iii), the premultiplied spectrum increases with the wavenumber,

$$k_x^+\phi_{uu}^+(k_x) = \Lambda_s\frac{k_x}{2\pi}. \tag{3.12}$$

The parameter Λ_s is a large-scale characteristic wavelength estimated as $\Lambda_s = A(z)U_\tau/f_C$, where f_C is the Coriolis frequency (Rossby & Montgomery 1935) ($f_C = 9.38 \times 10^{-5}$ Hz for the present data set), the parameter A is linearly proportional to z within the ESL, while Λ_s reaches the maximum value at the height of the ESL, then decreases (Högström *et al.* 2002).

The model of Högström *et al.* (2002) defined through (3.9), (3.11) and (3.12) allows for calculating the boundaries of region (ii). Specifically, from $A(z)$ and A_1, the non-dimensional low-wavenumber limit of region (ii), F, can be found by equating (3.11) and (3.12),

$$F = \frac{2\pi f_C A_1 \Delta_E}{A(z)U_\tau}. \tag{3.13}$$

Similarly, the wavenumber at the intersection between regions (i) and (ii) is found by equating (3.9) and (3.11),

$$P = \frac{1}{\kappa}\left(\frac{\alpha_K\varphi_\varepsilon^{2/3}}{A_1}\right)^{3/2}. \tag{3.14}$$

Building upon the spectral model proposed by Högström *et al.* (2002), we propose to further divide region (ii) into two high- and low-wavenumber sub-regions referred to as (ii$_A$) and (ii$_B$), respectively, where the energy contribution of wall-attached eddies (type-$\mathcal{A}$ eddies) is predominant for the former, while that associated with type-$\mathcal{B}$ eddies is predominant for the latter (see figure 5). This approach is inspired by previous works;

for instance, Rosenberg *et al.* (2013) and Vallikivi *et al.* (2015) modelled separately the VLSM spectral peak through a Gaussian function (here associated with region (ii$_B$)) and the flat premultiplied region through a cubic spline. For our study, the non-dimensional wavenumber at the intersection between regions (ii$_A$) and (ii$_B$), indicated with G in figure 5, is thought to scale with Δ_E considering that its spectral value is affected by the energy content of type-$\mathcal{B}$ eddies, which scale with Δ_E. Finally, the maximum height where region (ii$_A$) can be observed, z_{max}, is identified where the condition $P = z_{max}G/\Delta_E$ is fulfilled.

The technical strategy for the quantification of F, G, and P from the premultiplied streamwise velocity spectrum is detailed in the following. Starting from region (i), the term $\alpha_K/\kappa^{2/3}$ in (3.9) is fitted by overlapping the premultiplied streamwise velocity spectra versus the inertia-scaled wavenumber for all the heights probed by the LiDAR and over the frequency range $k_x z \geq 2$. The fitting of the experimental spectra leads to an estimate of $\alpha_K/\kappa^{2/3} = 0.60$ for the present data set.

For region (ii$_A$), A_1 is heuristically determined for each height in the proximity of the spectral range where the high-frequency limit P is expected ($k_x z \approx 1$). Subsequently, the intersection between the horizontal line equal to A_1 and the fitted spectrum for region (i) leads to the identification of the high-wavenumber limit P.

For region (iii), $A(z)$ is obtained for each height through the fitting of the streamwise velocity energy spectra with (3.12) limited to the low-frequency energy-increasing portion. Then, for each height, the intersection between the horizontal line equal to A_1 and the fitted spectrum for region (iii) identifies the low-frequency limit F. Finally, the inner boundary between regions (ii$_A$) and (ii$_B$), G, is heuristically quantified at the crossing between the energy-decreasing region for smaller wavenumbers typically associated with VLSMs and the horizontal line equal to A_1.

3.3. *Identification of the energy associated with different eddy typology based on the LCS of the streamwise velocity*

The scale-dependent cross-correlation of two statistically stationary velocity signals collected at wall-normal positions z and z_R (reference height) can be estimated through the two-point LCS,

$$\gamma^2(z, z_R; k_x) = \frac{|\phi'_{uu}(z, z_R; k_x)|^2}{\phi_{uu}(z; k_x)\phi_{uu}(z_R; k_x)}, \tag{3.15}$$

where $||$ indicates the modulus while $\phi'_{uu}(z, z_R; k_x)$ is the cross-spectral density of the two streamwise velocity signals, which is practically the Fourier transform of the cross-variance function between $u(z)$ and $u(z_R)$. Therefore, the LCS represents the fraction of common variance shared by $u(z_R)$ and $u(z)$ across frequencies (Bendat & Piersol 1986). Due to the normalization with the single-point energy spectra, we have $0 \leq \gamma^2 \leq 1$. Considering that the LCS is calculated from the amplitude of the cross-spectral density, no information is retained about the phase shift of the shared energy between the two velocity signals (Nelson, Hati & Howe 2013; Baars *et al.* 2017). This feature is advantageous when calculating the LCS from the LiDAR data, which are collected with a streamwise shift of about 18 m between consecutive LiDAR gates due to the elevation angle of 3.5° set for the LiDAR fixed scans. Nonetheless, it is reasonable to expect a slight reduction of γ^2 for a large height difference between z_R and z associated with the limitations in the applicability of the Taylor's hypothesis of frozen turbulence (Taylor 1938).

Considering a boundary layer flow encompassing only wall-attached eddies generated by a single hierarchy with wavelength λ_H, vertical size δ, and, thus, aspect ratio $\mathit{AR} = \lambda_H/\delta$, the non-zero portion of the LCS is limited to wall-normal positions with $z \leq \delta$, since no wall-attached eddies are present above, and to wavelengths with $\lambda_x \geq \lambda_H = \mathit{AR}\delta$ due to the concatenation and random repetitions of the same hierarchy along the streamwise direction (Baars *et al.* 2017). Therefore, the isolated-eddy contribution to the LCS for a single hierarchy can be modelled as

$$\gamma_H^2\left(\frac{\lambda_x}{\delta}, \frac{z}{\delta}\right) = C_0 H\left[1 - \frac{z}{\delta}\right] H\left[\frac{\lambda_x}{\mathit{AR}\delta} - 1\right]; \quad \text{as } \frac{z}{\delta} \leq 1, \quad \frac{\lambda_x}{\mathit{AR}\delta} \geq 1, \tag{3.16}$$

where H is the unit Heaviside function, while the parameter C_0 ($0 < C_0 < 1$) represents the isolated-eddy contribution to the LCS, and it only depends on the geometric features of the archetypal eddy. When a continuous distribution of attached eddies is considered, the resulting LCS will then be expressed as the sum of the various isolated contributions weighted by their probability density function throughout the scale range

$$\gamma^2\left(\frac{\lambda_x}{\Delta_E}; \frac{z}{\delta_{min}}, \frac{z}{\Delta_E}\right) = \min\left[\int_{\delta_{min}}^{\Delta_E} M\gamma_H^2\left(\frac{\lambda_x}{\delta}, \frac{z}{\delta}\right)\frac{\mathrm{d}\delta}{\delta}, 1\right], \tag{3.17}$$

where δ_{min} is equal to δ_1 or z_R if the latter is located in the near-wall or logarithmic region, respectively. Considering that

$$H\left[\frac{\lambda_x}{\mathit{AR}\delta} - 1\right] = H\left[\frac{z}{\delta} - \frac{\mathit{AR}z}{\lambda_x}\right], \tag{3.18}$$

(3.17) becomes

$$\gamma^2\left(\frac{\lambda_x}{\Delta_E}; \frac{z}{\delta_{min}}, \frac{z}{\Delta_E}\right) = \min\left\{\int_{z/\Delta_E}^{z/\delta_{min}} C_1 H\left[1 - \frac{z}{\delta}\right] H\left[\frac{z}{\delta} - \frac{\mathit{AR}z}{\lambda_x}\right]\frac{\delta}{z}\mathrm{d}\left(\frac{z}{\delta}\right), 1\right\}, \tag{3.19}$$

where $C_1 = MC_0$. Therefore, for a certain z and λ_x, the region where the contribution to the LCS is non-zero depends on the values of Δ_E, δ_{min} and AR. Specifically, four combinations are possible among these limits, each of them schematically reported in figure 6. For instance, assuming a wall-normal location within the logarithmic region ($z \geq \delta_1$) and $\mathit{AR}z \leq \lambda_x \leq \mathit{AR}\Delta_E$, the case reported in figure 6(*a*) is obtained, where the active boundaries of the non-zero contribution to the LCS are $\mathit{AR}z/\lambda_x$ and 1. Thus, (3.19) becomes

$$\gamma^2 = \min\left\{\int_{\mathit{AR}z/\lambda_x}^{1} C_1\frac{\delta}{z}\mathrm{d}\left(\frac{z}{\delta}\right), 1\right\} = \min\left\{C_1 \log\left(\frac{\lambda_x}{\mathit{AR}z}\right), 1\right\}, \tag{3.20}$$

which is the model proposed by Baars *et al.* (2017). This case, together with the three remaining combinations between active boundaries of (3.19) (sketched in figure 6*b–d*), lead to the analytical formulation of the LCS for an attached-eddy flow.

In Baars *et al.* (2017) it was noted that the LCS becomes zero for heights below Δ_E. To encompass this feature, an offset for γ^2, denoted as C_3, is added to the analytical

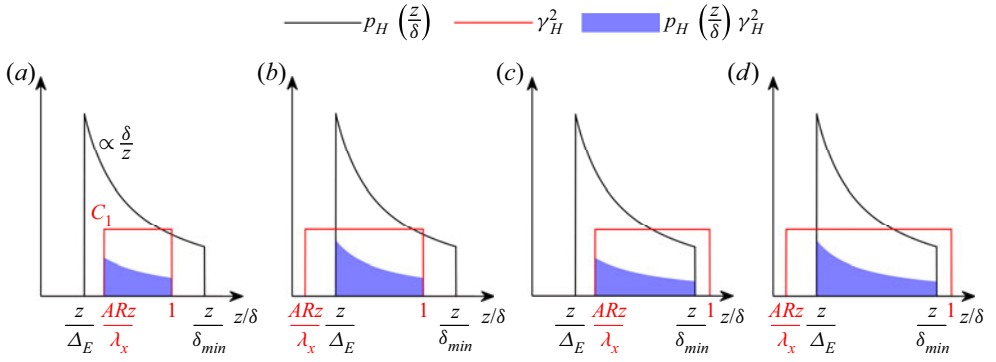

Figure 6. Isolated-eddy contribution to the LCS, γ_H^2 (3.16), p.d.f. of an isolated eddy with vertical extent δ, p_H, and their product for the various combinations of Δ_E, δ_{min} and AR. The various functions reported on the vertical axis are listed in the legend.

formulation of the LCS model developed from (3.19), which then reads as

$$\gamma^2 = \begin{cases} \min\left[C_1 \log\left(\dfrac{\lambda_x}{\mathit{AR}z}\right), 1\right] & \text{if } z \geq z_R, \quad \lambda_x/\Delta_E \leq \exp\left(\dfrac{C_3}{C_1}\right)\mathit{AR}\ (a), \\ \min\left[-C_1 \log\left(\dfrac{z}{\Delta_E}\right) + C_3, 1\right] & \text{if } z \geq z_R, \quad \lambda_x/\Delta_E > \exp\left(\dfrac{C_3}{C_1}\right)\mathit{AR}\ (b), \\ \min\left[C_1 \log\left(\dfrac{\lambda_x}{\mathit{AR}\delta_{min}}\right), 1\right] & \text{if } z < z_R, \quad \lambda_x/\Delta_E \leq \exp\left(\dfrac{C_3}{C_1}\right)\mathit{AR}\ (c), \\ \min\left[C_1 \log\left(\dfrac{\Delta_E}{\delta_{min}}\right) + C_3, 1\right] & \text{if } z < z_R, \quad \lambda_x/\Delta_E > \exp\left(\dfrac{C_3}{C_1}\right)\mathit{AR}\ (d). \end{cases} \tag{3.21}$$

The threshold wavelength $\lambda_x^{th}/\Delta_E = \exp(C_3/C_1)\mathit{AR}$ is obtained enforcing continuity in λ_x between (3.21a) and (3.21b), and it represents the boundary between wall-attached eddies and coherent structures generated from their streamwise concatenation. It is noteworthy that including C_3 implies $\gamma^2 = 0$ at $z_{max}/\Delta_E = \exp(C_3/C_1)$, rather than at $z/\Delta_E = 1$. In Baars *et al.* (2017), $\gamma^2 = 0$ was identified for $z \gtrapprox 0.7\Delta_E$ while the authors estimated $C_1 = 0.302$, which leads to $C_3 = -0.103$.

All the cases in (3.21) were observed experimentally in Baars & Marusic (2020a), and it is shown here that they are consistent with a continuous distribution of wall-attached eddies. In particular, assuming z_R within the near-wall region, we have $\delta_{min} = \delta_1$ and (3.21) becomes (4.7) of Baars & Marusic (2020a). Similarly, assuming z_R within the logarithmic region we have $\delta_{min} = z_R$, which leads to (4.10) of Baars & Marusic (2020a).

It is noteworthy that in Baars & Marusic (2020a), C_1 and AR are calibrated twice from the experimental distribution of LCS depending on whether the reference height was located in the near-wall or logarithmic region. Specifically, it was estimated $C_1 = 0.302$ and $\mathit{AR} = 14.01$ if z_R resides in the near-wall region and $C_1 = 0.383$ and $\mathit{AR} = 13.18$ if z_R resides in the logarithmic region. This discrepancy is attributed by Baars & Marusic (2020a) to the use of a single convection velocity for the application of the Taylor's hypothesis for frozen turbulence. From the proposed LCS model, we confirm that C_1 should not change with the reference height assuming a constant AR.

3.4. *Notes on the LCS of the streamwise velocity*

By considering the logarithmic coordinates $\lambda^* = \log(\lambda_x/\Delta_E)$ and $z^* = \log(z/\Delta_E)$, the LCS model of (3.21) can be rewritten, by only considering the case with $\gamma^2 \leq 1$, as

$$\gamma^2 = \begin{cases} C_1\left(\lambda^* - \lambda^*_{th}\right) - C_1\left(\Delta z^* + z^*_R\right) + C_3 & \text{if } \Delta z^* \geq 0, \quad \lambda^* \leq \lambda^*_{th}\ (a), \\ -C_1\left(\Delta z^* + z^*_R\right) + C_3 & \text{if } \Delta z^* \geq 0, \quad \lambda^* > \lambda^*_{th}\ (b), \\ C_1\left(\lambda^* - \lambda^*_{th}\right) - C_1 z^*_R + C_3 & \text{if } \Delta z^* < 0, \quad \lambda^* \leq \lambda^*_{th}\ (c), \\ -C_1 z^*_R + C_3 & \text{if } \Delta z^* < 0, \quad \lambda^* > \lambda^*_{th}\ (d), \end{cases} \tag{3.22}$$

where $\lambda^*_{th} = C_3/C_1 + \log(\mathit{AR})$ and $\Delta z^* = \log(z/z_R)$. Based on (3.22), the following considerations can be made.

(a) For $\lambda^* \leq \lambda^*_{th}$, γ^2 is a linear function of λ^*, its slope is not a function of z^* and has a constant value equal to C_1.
(b) For $\lambda^* > \lambda^*_{th}$, γ^2 achieves an asymptotic value, γ^2_∞, which is a linear function of Δz^* with slope $-C_1$ if $\Delta z^* \geq 0$ while it is constant for $\Delta z^* < 0$.
(c) The threshold wavelength, λ^*_{th}, is not a function of z^*.
(d) The intercept of γ^2 for $\lambda^* \leq \lambda^*_{th}$ is equal to the asymptotic value achieved for $\lambda^* > \lambda^*_{th}$ for every z^*.

By imposing $\gamma^2 = 0$ in (3.21), we obtain the boundary conditions for a non-null LCS,

$$\begin{cases} z^* = \lambda^* - \log(\mathit{AR}) & \text{if } \Delta z^* \geq 0, \quad \lambda^* \leq \lambda^*_{th}\ (a), \\ z^* = C_3/C_1 & \text{if } \Delta z^* \geq 0, \quad \lambda^* > \lambda^*_{th}\ (b), \\ \lambda^* = z^*_R + \log(\mathit{AR}) & \text{if } \Delta z^* < 0, \quad \lambda^* \leq \lambda^*_{th}\ (c), \\ z^*_R = C_3/C_1 & \text{if } \Delta z^* < 0, \quad \lambda^* > \lambda^*_{th}\ (d). \end{cases} \tag{3.23}$$

The relationship (3.23*a*) represents the line separating the coherent from the non-coherent component of the flow with z_R in the (λ_x, z) domain. According to the LCS model, this line represents the spectral boundary between region (i) and region (ii$_A$) for wall-normal positions above z_R. Below z_R, the zero contour of γ^2 has a constant value of λ_x (3.23*c*) because, according to the AEH, eddies with a height smaller than z_R do not contribute to the LCS. It is noteworthy that the spectral boundary between region (i) and region (ii$_A$) is only a function of AR, and it shifts towards larger wavelengths as AR increases.

The remaining relationships obtained by imposing $\gamma^2 = 0$ provide z_{max} for $\lambda^* > \lambda^*_{th}$ in (3.23*b*), and the trivial condition that z_R should be lower than z_{max} to achieve a non-null γ^2 (3.23*d*).

Similarly, we can estimate the conditions for the saturation on the contribution of wall-attached eddies to the LCS by imposing $\gamma^2 = 1$ in (3.21),

$$\begin{cases} z^* = \lambda^* - \log(\mathit{AR}) - 1/C_1 & \text{if } \Delta z^* \geq 0, \quad \lambda^* \leq \lambda^*_{th}\ (a), \\ z^* = (C_3 - 1)/C_1 & \text{if } \Delta z^* \geq 0, \quad \lambda^* > \lambda^*_{th}\ (b), \\ \lambda^* = z^*_R + \log(\mathit{AR}) + 1/C_1 & \text{if } \Delta z^* < 0, \quad \lambda^* \leq \lambda^*_{th}\ (c), \\ z^*_R = (C_3 - 1)/C_1 & \text{if } \Delta z^* < 0, \quad \lambda^* > \lambda^*_{th}\ (d). \end{cases} \tag{3.24}$$

From (3.24*a*), it is noted that the line demarcating the LCS saturation above z_R is parallel to that separating the spectral region (i) from (ii$_A$), yet translated towards larger wavelengths by $\Delta\lambda^* = 1/C_1$. The same shift applies below z_R (3.24*c*), which provides an insightful

physical interpretation for C_1, namely C_1 controls the spectral width where the energy contributions due to wall-attached eddies build up. Furthermore, (3.24*b*) and (3.24*d*) provide the maximum wall-normal position and the maximum z_R where LCS saturation is achieved for $\lambda^* > \lambda^*_{th}$. Further, the range in the wall-normal position where the LCS is non-null is equal to $\Delta z^* = 1/C_1$.

4. Detection of the energy associated with eddies of different typology from LiDAR measurements

4.1. *Energy spectra of the streamwise velocity*

As detailed in Appendix A, the spectral gap between mesoscales and turbulent scales is identified at a frequency $f_{\text{gap}} = 0.0055$ Hz, which corresponds to a time period of about 182 s, while the outer scale of turbulence is estimated as $\Delta_E = 127$ m. Therefore, the friction Reynolds number for the data set under investigation is equal to $Re_\tau = U_\tau \Delta_E/\nu = 3.55 \times 10^6$. The streamwise velocity signals collected through the wind LiDAR and the sonic anemometer are high-pass filtered with a cutoff frequency equal to f_{gap} through the filter proposed by Hu *et al.* (2020) to isolate only velocity fluctuations connected with turbulence motions.

The streamwise velocity energy spectra are calculated through the Welch algorithm (Welch 1967) using a window size equal to 0.0003 Hz and 10 % overlapping. Each spectrum is evaluated over $N/2 + 1$ frequencies linearly spaced between 0 and the Nyquist frequency (0.5 Hz for the LiDAR signals and 10 Hz for the sonic-anemometer measurements), where N is the total number of samples of the velocity signals (3580 and 72 000 for LiDAR and sonic-anemometer data, respectively). The spectra are then smoothed using a moving average applied at each frequency f_i using a variable spectral stencil of $f_i \pm 0.35 f_i$ (Baars & Marusic 2020*a*). The obtained streamwise velocity premultiplied energy spectra are reported in figure 7 versus the outer-scaled wavenumber and the wall-normal distance. The wavenumber is calculated as $k_x = 2\pi f/U(z)$ by leveraging the Taylor's hypothesis of frozen turbulence (Taylor 1938), where f is frequency. At the lowest heights, significant energy content is observed within a λ_x range between $0.3\Delta_E$ and $8\Delta_E$ ($0.9 \lessapprox k_x\Delta_E \lessapprox 20$). This energy contribution reduces with increasing height, while for heights with $z/\Delta_E \gtrapprox 0.1$, the dominant energy contributions reside within the wavelength range between $10\Delta_E$ and $20\Delta_E$.

As mentioned in § 3.2, from the streamwise velocity premultiplied spectra calculated at each height, A_1 is estimated heuristically, while the parameter $A(z)$ is obtained by fitting the spectrum with (3.12) over the spectral region (iii). An example of this procedure is reported in figure 8(*a*) for the premultiplied streamwise velocity spectrum evaluated for the LiDAR data collected at a height of 16 m. A spectral region with roughly constant energy, i.e. corresponding to region (ii$_A$), is identified in the proximity of the low-frequency limit of region (i) ($k_x\Delta_E \approx 5$). The fitting of (3.9) for the model of region (i) with the experimental spectrum is reported with a dashed line over the high-frequency part of the spectrum, while the fitting with (3.12) for the model of region (iii) is also reported with a dashed line over the low-frequency part of the spectrum. The intersections between the horizontal dashed line corresponding to the identified value of A_1 ($\approx$0.91 for the LiDAR data reported in figure 8*a*) and the modelled spectra for regions (i) and (iii) enable the identification of the non-dimensional spectral limit P (red circle in figure 8*a*) and F (blue triangle in figure 8*a*), respectively. Finally, for the identification of the spectral limit G, the part of region (ii) with energy larger than A_1 yet reducing with increasing wavenumber is considered. The spectral

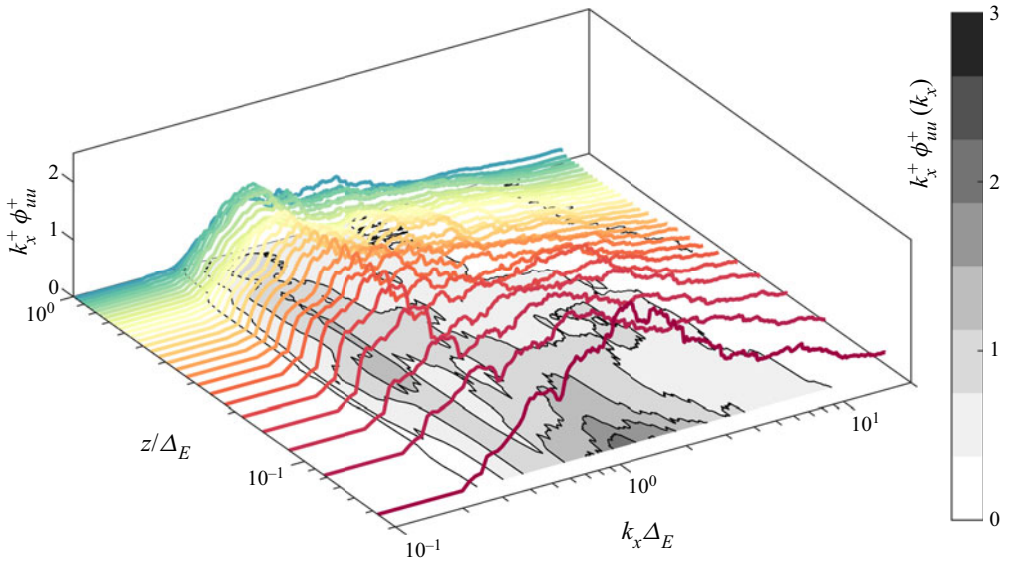

Figure 7. Premultiplied energy spectra of the streamwise velocity obtained from the wind LiDAR measurements.

limit G is associated with the intersection of this part of the spectrum with the horizontal dashed line corresponding to A_1.

The vertical profiles of the spectral limits P, G and F obtained from the analysis of the premultiplied streamwise velocity energy spectra are reported in figure 8(*b*). First, it is observed that, as predicted from the AEH (see § 1), the non-dimensional spectral limits G and F are roughly invariant with z. Specifically, G has a mean value of about 3.3, which corresponds to a wavelength of $1.9\Delta_E$, while F has a mean value of 0.44, which corresponds to a wavelength of $14.3\Delta_E$. In contrast, the spectral limit between region (i) and region (ii$_A$), P, decreases with the wall-normal position, which confirms its inertial-scaling consistently with the predictions of Perry & Chong (1982), Perry *et al.* (1986) and the experimental results of Nickels *et al.* (2005), Hwang (2015), Baars *et al.* (2017) and Hu *et al.* (2020) for laboratory flows. The linear fitting of the profile reported in figure 8(*b*) produces an estimate for P of 0.58, which corresponds to an eddy aspect ratio of $\lambda_x/z = 2\pi/0.58 \approx 10.8$, which is smaller than the value of 14 estimated in Baars *et al.* (2017) through the LCS analysis of data sets collected with a wide range of Reynolds number flows, including an ASL case as well.

As mentioned in § 3.2, the intersection between $P\Delta_E/z$ and G identifies the maximum height where region (ii$_A$) is observed, i.e. $z_{max} \approx 21$ m ($0.17\Delta_E$). It is noteworthy that this outer-scaled value coincides with that provided by Hwang (2015) and it is close to the results by Baars & Marusic (2020*b*) ($0.15\Delta_E$), while it is lower than the value proposed by Hu *et al.* (2020) ($0.53\Delta_E$).

In addition to the limits amongst the different spectral regions, it is important to analyse the vertical profile of the parameter A_1, which is heuristically estimated from the premultiplied spectra of the streamwise velocity. In the perspective of the AEH, A_1 can be estimated only for wall-normal positions lower than z_{max}, namely for heights where the spectral region (ii$_A$) can be detected. However, in this work, a value is still associated with A_1 even aloft, which corresponds to the average energy within the spectral range between regions (i) and (iii). The obtained wall-normal profile of A_1 is reported in

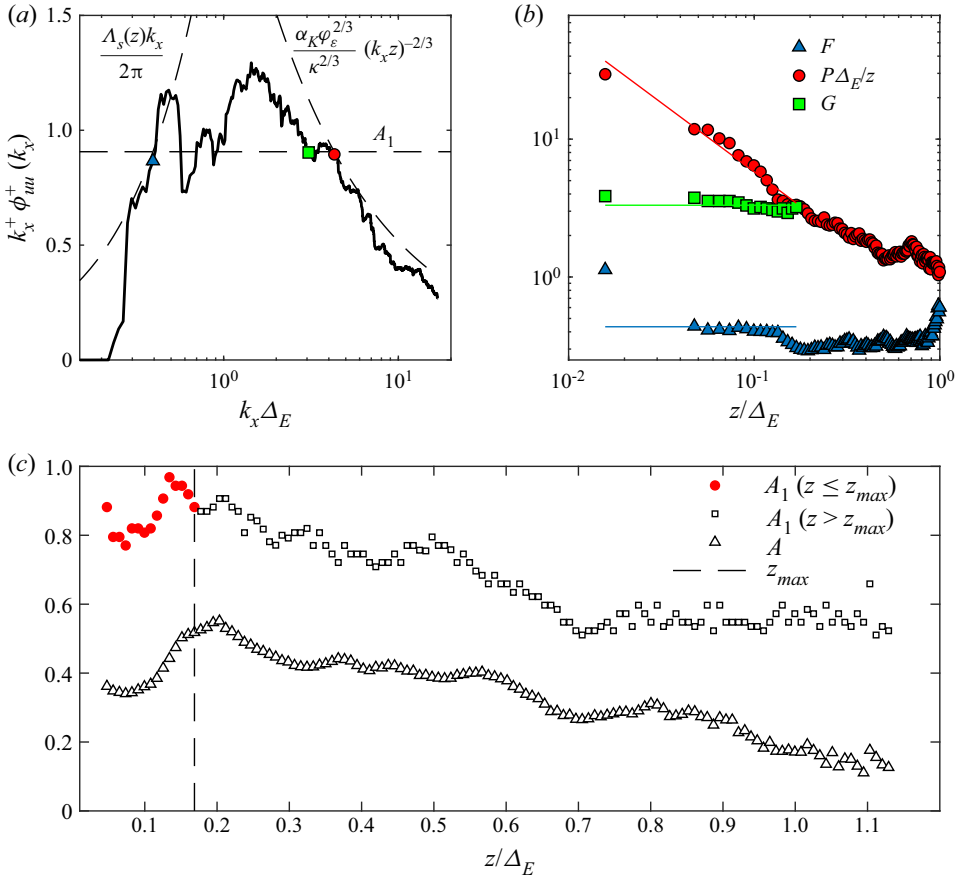

Figure 8. Identification of spectral limits from the streamwise velocity energy spectra. (*a*) Detection of the spectral limits for the LiDAR velocity signal collected at a 16 m height. (*b*) Wall-normal profiles of F, G and P. (*c*) Vertical profiles of A_1 (red circles for $z \le z_{max}$ and black squares for $z > z_{max}$) and A.

figure 8(*c*), specifically reporting values for heights below z_{max} with red circles and aloft with black squares. Starting from the lowest height and moving upwards, A_1 increases from a value of about 0.8 up to about 1 at $z/\Delta_E \approx 0.13$. While the obtained values are reasonable according to previous works (e.g. $A_1 = 0.80$ for channel flows and $A_1 = 1.0$ for ASL and boundary layers (Hu *et al.* 2020), while $A_1 = 0.975$ for boundary layers Baars & Marusic 2020*b*), the variability of A_1 with height is not in agreement with the AEH predictions. Furthermore, for wall-normal positions above z_{max}, the mean energy roughly monotonically reduces up to $z/\Delta_E \approx 0.7$, then it remains roughly constant aloft.

An interpretation of these experimental results might be provided by analysing the vertical profile of the parameter $A(z)$, which represents the energy level over region (iii) as a function of height and it is connected with the vertical variability of the turbulent kinetic energy associated with large-scale turbulent motions. Figure 8(*c*) shows that $A(z)$ increases from 0.37 up to 0.60 between $0.1\Delta_E$ and $0.2\Delta_E$, followed by a roughly monotonic decrease aloft. These values are comparable to those reported by Högström *et al.* (2002), namely $A(z)$ increases from 0.2 up to 1 at a height of $z = 0.3\Delta_E$, then it decreases aloft. The similar trends obtained for A_1 and $A(z)$ as a function of the wall-normal position suggest that even though a roughly flat region of the premultiplied spectra can be singled out over

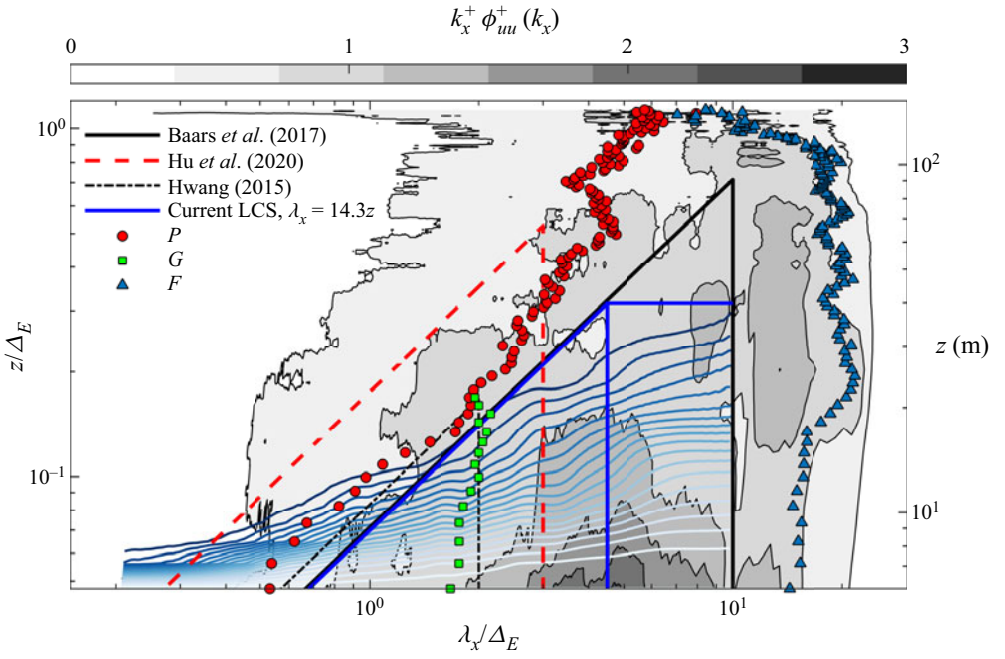

Figure 9. Premultiplied energy spectra of the LiDAR streamwise velocity measurements reported as a grey colour map (isocontour levels from 0.4 up to 3 with a 0.4 step). The LCS are reported as blue-scaled contour lines (isocontour levels from 0.1 up to 1 with a 0.05 step).

the region (ii$_A$), the values attained by A_1 can significantly be affected by an underlying energy contribution associated with VLSMs, which is a reasonable feature within region (ii) where wall-attached and coherent structures with larger wavelengths co-exist and, thus, their energy contributions overlap.

To better visualize the boundaries of the various spectral regions, the streamwise velocity premultiplied energy spectra are reported in figure 9 with a grey colour map. The estimated spectral limits for the different heights, *P*, *G* and *F*, are reported as well with red circle, green square and blue triangle markers, respectively. The spectral limits of region (ii) estimated from the above-mentioned previous works are also reported in that figure. For heights below $0.17\Delta_E$, the wall-normal trend of the spectral limit *P* has a good level of agreement with the findings for channel flows by Hwang (2015), where the aspect ratio of the wall-attached eddies was estimated as $\mathcal{AR} = 12$. The present results for *P* are slightly larger than the spectral limit estimated through the LCS in Baars *et al.* (2017), where the authors estimated $\mathcal{AR} = 14$ for boundary layers.

From the analysis of the spectral limit *G* between regions (ii$_A$) and (ii$_B$) (green squares in figures 8(*b*) and 9), the average value of $\lambda_x = 1.9\Delta_E$ is close to that obtained by Hwang (2015) ($\lambda_x = 2\Delta_E$). For the spectral limit between regions (ii) and (iii), the outer-scaled wavelength associated to *F* (blue triangles in figures 8(*b*) and 9) is quantified as $14.3\Delta_E$ below z_{max} and $15.8\Delta_E$ above, both within the interval provided by Hutchins *et al.* (2012) for the maximum streamwise extent of VLSMs in a boundary layer, i.e. between $10\Delta_E$ and $20\Delta_E$. Finally, the comparison for the spectral limits of region (ii) obtained from the current investigation with those from previous studies (Hwang 2015; Baars *et al.* 2017; Hu *et al.* 2020) are summarized in table 2.

Reference	Flow type	z_{max}/Δ_E	Limits k_x^{-1} region	P	G	F
Baars *et al.* (2017)	TBL, CH, ASL	—	$14z \leq \lambda_x \leq 10\Delta_E$	0.45	0.63	—
Hu *et al.* (2020)	TBL, CH, ASL	0.53	$5.7z \leq \lambda_x \leq 3\Delta_E$	1.10	2.09	—
Hwang (2015)	CH	0.17	$12z \leq \lambda_x \leq 2\Delta_E$	0.52	3.14	—
Nickels *et al.* (2005)	TBL	0.02	$15.7z \leq \lambda_x \leq 0.3\Delta_E$	0.40	20.94	—
Present spectra	ASL	0.17	$10.8z \leq \lambda_x \leq 1.9\Delta_E$	0.58	3.30	0.44
Present LCS	ASL	0.31	$14.3z \leq \lambda_x \leq 4.5\Delta_E$	0.44	1.40	—

Table 2. Identification of the various regions from the energy spectra and LCS of the streamwise velocity. The acronyms TBL, CH and ASL stand for turbulent boundary layer, channel flow and atmospheric surface layer, respectively.

4.2. *Detection of different energy contributions in the LiDAR measurements through the LCS*

The energy contributions associated with different eddy typologies are further investigated through the analysis of the LCS, which is calculated according to (3.15) through the Welch (1967) algorithm and leveraging as reference the velocity signal collected from the lowest LiDAR gate ($z_R \approx 0.05\Delta_E$). Specifically, each signal is subdivided into windows with a 179 s duration (corresponding to nearly $18\Delta_E$ leveraging the Taylor's hypothesis of frozen turbulence Taylor 1938) and 90 % overlapping between consecutive windows to estimate the auto- and cross-spectra of the streamwise velocity. It is noted that the values for the window duration and overlapping of the various data subsets do not distort the LCS at lower frequencies, while these parameters are more important for ensuring a roughly null LCS at higher frequencies. Each LCS is smoothed, as performed for the energy spectra. For more details on the calculation of the LCS and the determination of its parameters see Appendix C. The LCS calculated from the LiDAR measurements is reported as blue isocontours over the (λ_x, z) domain in figure 9.

The parameters of the analytical LCS model for wall-attached eddies (3.21) are quantified by fitting the LCS calculated from the LiDAR measurements. According to the point (b) discussed in § 3.4, for a fixed λ_x, γ^2 is a linear function of $\log(z/z_R)$ with a slope equal to $-C_1$ for heights above z_R. To this aim, λ_x is selected within the interval between $3.5\Delta_E$ and $9.5\Delta_E$ to avoid effects due to small-wavelength eddies and large-wavelength non-turbulent contributions, respectively. The portions of γ^2 varying roughly linearly with $\log(z/z_R)$, which are reported with a red colour scale in figure 10(a), are fitted with a linear function of $\log(z/z_R)$ to estimate the intercept I and the slope $-C_1$, which are then reported in figure 10(b) with square and circle markers, respectively. Here C_1 has roughly constant values for different λ_x, as predicted from the analytical model for the LCS of (3.22), with an average value of $C_1 = 0.485$.

For $z \geq z_R$, the analytical LCS model predicts that the intercept of γ^2, I, should be a linear function of $\log(\lambda_x)$ for $\lambda_x \leq \lambda_x^{th}$, while achieving an asymptotic value equal to C_3 for $\lambda_x > \lambda_x^{th}$ (3.22). In figure 10(b) the values of I confirm these predictions, specifically showing an asymptotic value of the intercept of $C_3 \approx -0.56$ for $\lambda_x/\Delta_E \geq 4.5$, thereby assumed as λ_x^{th}. An assessment of the results obtained with this fitting procedure is performed considering that the intercept of γ^2 should vary as $C_1 \log(\lambda_x/\lambda_x^{th}) + C_3$ for $\lambda_x \leq \lambda_x^{th}$ and $z \geq z_R$. This function, which is reported in figure 10(b) with a black solid line using the fitted values obtained for C_1 and C_3, and λ_x^{th} shows a good agreement with the experimental data considering the small number of samples available for $\lambda_x \leq \lambda_x^{th}$.

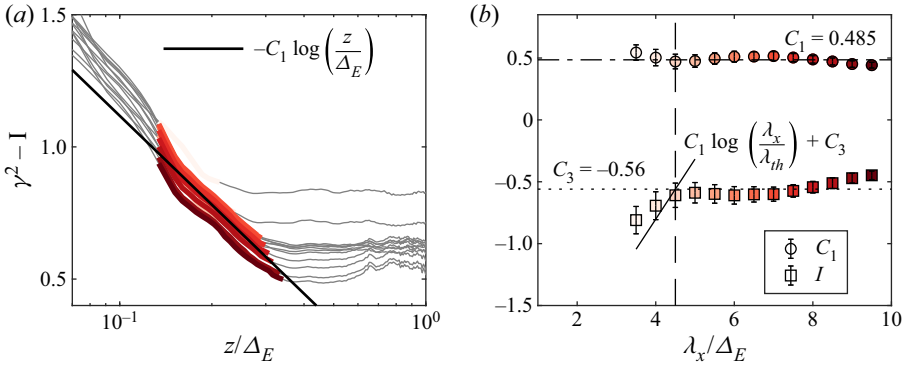

Figure 10. LCS of the LiDAR measurements using $z_R/\Delta_E \approx 0.05$; (*a*) $\gamma^2 - I$ for fixed values of λ_x; (*b*) fitted values of C_1 and I from (3.22), the error bars refer to 95 % confidence level. The parameter λ_x^{th} is reported with a vertical dashed line.

Recalling that $\log(\lambda_x^{th}/\Delta_E) = C_3/C_1 + \log(\mathit{AR})$, we can estimate the aspect ratio of the coherent eddies as $\mathit{AR} \approx 14.3$. Finally, the maximum height attained by wall-attached eddies is estimated from (3.23*b*), namely $z_{max}/\Delta_E = \exp(C_3/C_1) \approx 0.31$. This estimate of z_{max} obtained from the LCS analysis is larger than that obtained from the analysis of the energy spectra, i.e. $0.17\Delta_E$ (§ 4.1), as well as the estimates obtained by Hwang (2015) and Baars & Marusic (2020*b*) ($0.17\Delta_E$ and $0.15\Delta_E$, respectively); furthermore, the spectral approach of Hu *et al.* (2020) returns a sensibly larger value of z_{max} ($0.53\Delta_E$). Finally, in Baars *et al.* (2017), for an aspect ratio of 14, the authors estimated $\lambda_x^{th} = 10\Delta_E$ based on $z_{max} = 0.71\Delta_E$.

The estimate of $z_{max}/\Delta_E \approx 0.31$ obtained from the LCS analysis agrees with the vertical extent of the ESL for ASL flows, which was previously estimated equal to $0.3\Delta_E$ (Hunt & Morrison 2000; Högström *et al.* 2002; Drobinski *et al.* 2007). In the existing literature, the ESL is considered as the layer where the vertical confinement induced by the wall affects the dynamics and evolution of eddies entraining the boundary layer from aloft that, in turn, contribute to the generation of new turbulence structures from the wall. Our analysis seems to indicate that the ESL is dominated by a hierarchical distribution of eddies statistically attached to the wall.

The calibrated LCS model, and specifically the $\gamma^2 = 0$ condition (3.23*a*), is now compared with the experimental values of γ^2, as reported in the colour map of figure 9. Analysing the darkest isocontour with $\gamma^2 = 0.1$, a deviation from the predicted unitary slope of the LCS isocontours is observed for $z \lessapprox 0.12\Delta_E$, which is due to the local contribution of small, wall-incoherent structures (type-$\mathcal{C}$ eddies) (Krug *et al.* 2019; Baars & Marusic 2020*a*) as a consequence of the small vertical separation between z_R and the wall-normal position of these LiDAR data. Moving towards higher vertical positions and for $\lambda_x/\Delta_E \approx 2$, a unitary slope of the isocontours is recovered, in agreement with the LCS model (3.23*a*), and in agreement with previous experimental results (Baars *et al.* 2017; Baars & Marusic 2020*a*; Li *et al.* 2021). For higher wall-normal positions, a further deviation from the model prediction is observed, which may be ascribed to a residual thermal stratification still present in the ASL flow considering the early morning time of the data collection (local time between 3:00 AM and 4:00 AM), as already observed from previous field experiments (Krug *et al.* 2019).

It is noteworthy that the zero-LCS contour predicted with (3.23*a*) has a relatively good agreement with the vertical profile of the spectral limit P between regions (i) and (ii$_A$)

identified through the analysis of the streamwise velocity energy spectra in § 4.1 (figure 9), yet translated towards slightly larger wavelengths. An aspect ratio of 14.3 is estimated indeed from the LCS analysis, while $\mathcal{AR} \approx 10.8$ from the analysis of the energy spectra. Nonetheless, this result can be considered as proof that the inverse-power-law region of the streamwise velocity energy spectra is associated with wall-attached eddies (Perry *et al.* 1986), and the LCS approach resonates with the spectral approach to identify the k_x^{-1} high-frequency limit.

The LCS analytical model calibrated through the LiDAR data for the high-frequency limit (3.23*a*) is in good agreement with the analysis based on the LCS presented in Baars *et al.* (2017) for boundary layers ($\mathcal{AR} = 14$), while a slightly smaller aspect ratio ($\mathcal{AR} = 12$) was estimated in Hwang (2015) for channel flows. In contrast, the high-frequency spectral limit provided in Hu *et al.* (2020) with $\mathcal{AR} = 5.7$ seems to be an underestimate for the present data set.

Regarding the spectral boundary between the energy associated with wall-attached eddies and that due to larger coherent structures, the spectral limit G estimated through the analysis of the streamwise velocity energy spectra is about $1.9\Delta_E$, which is very similar to the respective limit estimated by Hwang (2015), and is significantly lower than the value of $4.5\Delta_E$ obtained from the present LCS analysis through λ_x^{th}. For the sake of completeness, G was estimated equal to $2.09\Delta_E$ in Hu *et al.* (2020) and $10\Delta_E$ in Baars *et al.* (2017) (estimated indirectly from $\mathcal{AR}$ and z_{max}). This analysis would suggest that the analysis of streamwise velocity energy spectra should lead to an underestimate of the spectral limit G due to the co-existence of energy contributions associated with eddies of different typologies. In contrast, the present LCS approach should offer a more reliable approach to separate wall-attached spectral energy from that associated with larger coherent structures.

Finally, the present LCS method does not provide a criterion to identify the low-frequency limit of the spectral region (ii$_B$), F, which is then only identifiable through the analysis of the streamwise velocity energy spectra.

4.3. *LCS calculated with increasing reference height*

Once the LCS analysis is performed with the reference height $z_R = 0.05\Delta_E$, a similar analysis is carried out by increasing z_R, which can provide more insights into the LCS analytical model (3.21), especially for $z < z_R$. However, we do not expect this analysis to further contribute to the foregoing discussion for $z > z_R$ because, with increasing z_R, the vertical range where incremental contributions associated with wall-attached eddies can be observed, $z_{max} - z_R$, reduces. To this aim, six additional reference heights are selected, namely $0.20\Delta_E$, $0.25\Delta_E$, $0.30\Delta_E$, $0.45\Delta_E$, $0.50\Delta_E$ and $0.70\Delta_E$.

The LCS maps obtained for all the considered z_R values are reported as isocontours in figure 11; further, the $\gamma^2 = 0$ isocontours estimated analytically through (3.23) are also reported using the parameters C_1, C_3 and $\mathcal{AR}$ calibrated as for § 4.2. For the region at smaller wavelengths demarcated by the analytically predicted $\gamma^2 = 0$ isocontours, it is evident that the experimental LCS obtained from the LiDAR measurements do not follow the analytical model of (3.21), rather they are dominated by energy contributions associated with wall-detached type-$\mathcal{C}$ eddies (Krug *et al.* 2019; Baars & Marusic 2020*a*). However, with increasing z_R, thus increasing the vertical distance between z_R and the lower LiDAR sampling heights, which is advantageous to reduce the effects of type-$\mathcal{C}$ eddies on the LCS, a roughly vertical $\gamma^2 = 0$ isocontour is observed already for $z_R/\Delta_E = 0.2$, which is even more evident for $z_R/\Delta_E = 0.25$ and 0.3. As predicted through the LCS analytical model (3.23*c*), for $z < z_R$, the $\gamma^2 = 0$ isocontour should occur for $\lambda_x = \mathcal{AR}z_R$, which is indeed in good agreement for all the z_R values used for this analysis below z_{max}

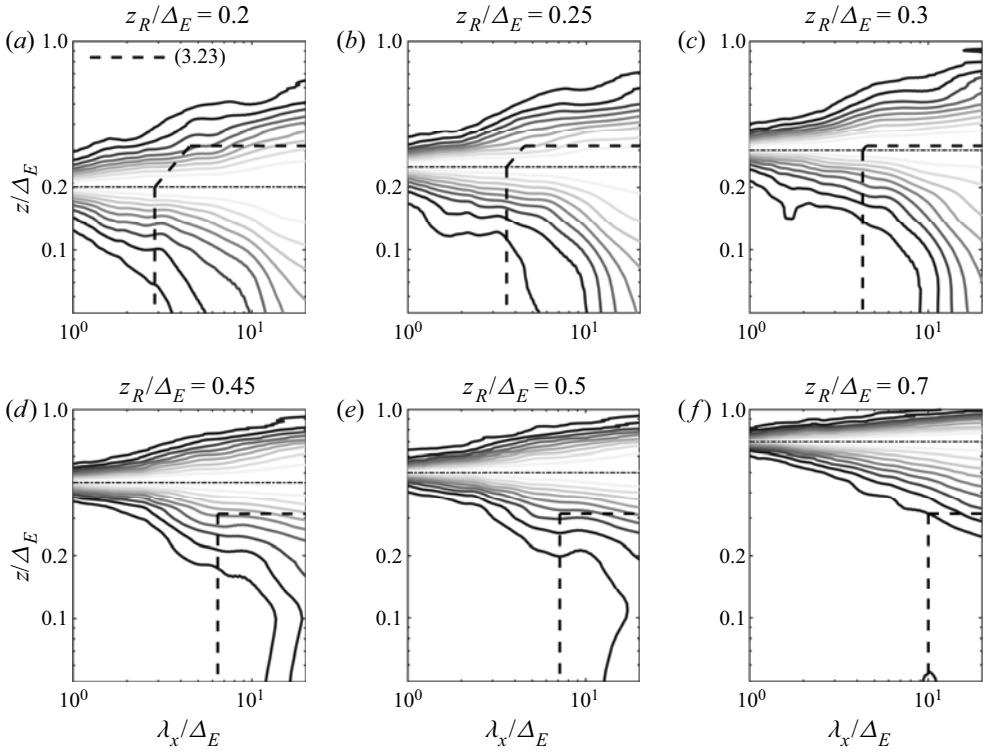

Figure 11. Isocontours (values from 0.1 up to 1 with a step of 0.1) of the LCS obtained with different z_R (horizontal dot-dashed lines). The $\gamma^2 = 0$ contours predicted through the model in (3.23) are reported with a dashed line.

by assuming $\mathcal{R} = 14.3$ as estimated in § 4.2. The vertical $\gamma^2 = 0$ isocontour becomes less evident with increasing z_R, until it disappears completely for $z_R/\Delta_E = 0.7\Delta_E$, indicating that no structures originating from below $z_R = 0.7$ are coherent with that reference position.

The maps of the streamwise velocity energy spectra for the coherent (figure 12) and incoherent (figure 13) components calculated for all the selected reference heights are now analysed. Starting from the lowest reference height, $z_R = 0.05\Delta_E$, it is observed that the coherent energy is practically confined within the $\gamma^2 = 0$ limit predicted in (3.23*a*) and the maximum height (3.23*b*) (figure 12*a*). The energy peak is observed at the lowest height ($z_R = 0.05\Delta_E$) at a wavelength $\lambda_x/\Delta_E \approx 5.2$. This is practically the upper region of the outer energy peak already observed by, e.g. Wang & Zheng (2016) for atmospheric flows.

On the other hand, figure 13(*a*) shows that the incoherent component obtained using $z_R = 0.05\Delta_E$ encompasses energy across the entire spectral range considered and up to Δ_E. Furthermore, the energy seems to move towards larger wavelengths with increasing height, which is a similar feature predicted from the AEH for wall-attached eddies. This suggests that also wall-detached eddies might be affected by the wall confinement of the flow and the local shear in the boundary layer. The incoherent energy component may be thought of as the footprint of shear surface layer structures entraining from above via top–down motions (Hunt & Morrison 2000; Högström *et al.* 2002; Morrison 2007); thus, incoherent with a reference height located in the ESL.

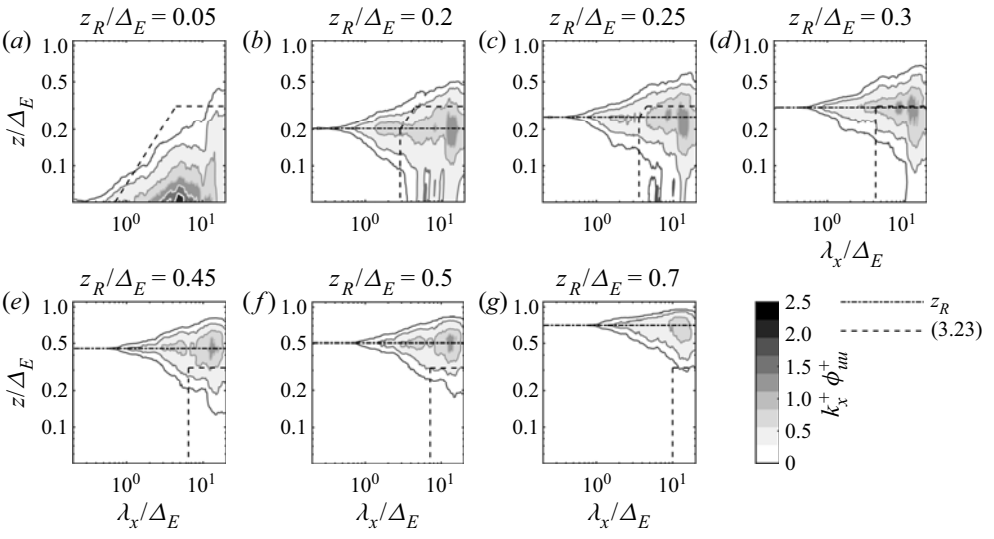

Figure 12. Coherent portion of the streamwise velocity energy spectra calculated for different reference heights, z_R.

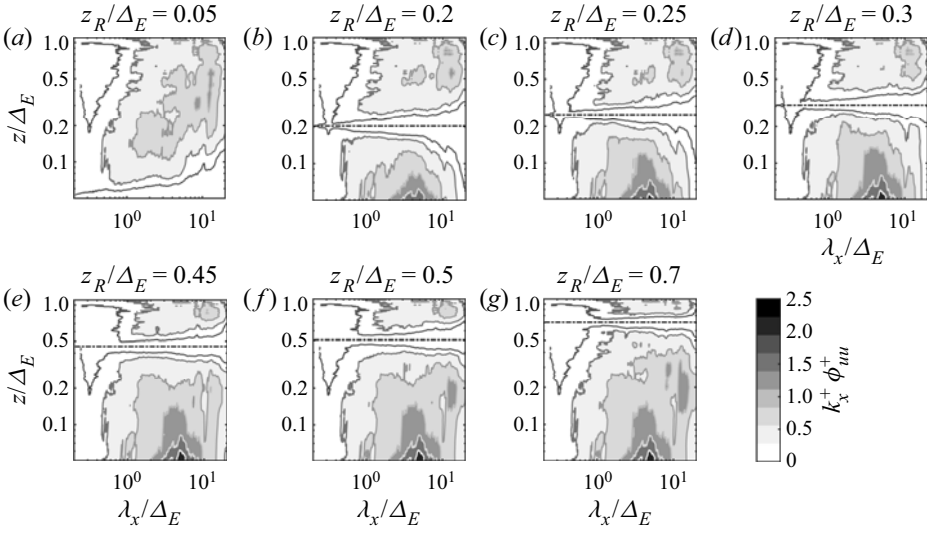

Figure 13. Incoherent portion of the streamwise velocity energy spectra calculated for different reference heights, z_R.

With increasing reference height, i.e. for $z_R = 0.2\Delta_E$, the coherent energy below z_R (figure 12*b*) drastically reduces compared with the case with $z_R = 0.05\Delta_E$ (figure 12*a*), and the remaining coherent energy is mainly located towards large wavelengths ($O(\lambda_x/\Delta_E) \approx 10$). This indicates that a cluster of coherent structures originated below $z_R = 0.2\Delta_E$, i.e. wall-attached eddies, does not attain this height, and only taller wall-attached eddies are left in the coherent energy component, which are characterized by larger wavelengths indeed.

For the same reason, increasing the reference height from $0.05\Delta_E$ to $0.2\Delta_E$ leads to enhanced incoherent energy below z_R (compare figure 13(*b*) with 13(*a*)). This added energy resembles the coherent energy obtained with $z_R = 0.05\Delta_E$ (figure 12*a*). Therefore, this analysis corroborates that the increase of reference height from $0.05\Delta_E$ to $0.2\Delta_E$ mainly leads to transferring a certain energy packet associated with wall-attached eddies from the coherent to the incoherent component.

It is noteworthy that in figure 12(*b*) a significant amount of coherent energy is singled out around $z_R = 0.2\Delta_E$, which is the effect on the LCS due to type-$\mathcal{C}$ eddies and their streamwise concatenation. A similar feature is observed for all the reference heights located above $0.05\Delta_E$ (figure 12*b–g*).

A similar trend is observed with increasing z_R below $z_{max} \approx 0.31\Delta_E$, i.e. reduced coherent energy and increased incoherent energy below z_R, while above z_{max}, i.e. in figure 12(*e–g*), the coherent component shows only the contribution associated with type-$\mathcal{C}$ eddies and no energy extending below, indicating no contribution due to wall-attached eddies. On the other hand, above z_{max}, the incoherent component achieves practically an asymptotic energy map for $z < z_{max}$, and only energy at large scales for $z > z_{max}$ are added with increasing z_R, which confirms that no wall-attached eddies are statistically present above z_{max}.

4.4. *Streamwise turbulence intensity*

The energy contributions to the streamwise velocity associated with wall-attached eddies and larger coherent structures have been identified through the analysis of the streamwise velocity energy spectra (§ 4.1), and the LCS (§ 4.2). Considering that the streamwise turbulence intensity is the integrated spectral energy across scales, it is then possible to distinguish the contributions to $\overline{uu}$ associated with eddies of different typologies. The streamwise turbulence intensity obtained using the integration limits estimated either from the spectral analysis (§ 4.1) or the LCS (§ 4.2) are reported in figure 14(*a*) with black and blue markers, respectively. Specifically, the streamwise turbulence intensity associated with wall-attached eddies, $\overline{uu}_{ii,A}$, is obtained by integrating the streamwise velocity energy spectra between the limits P and G for the spectral method, while for the LCS method, the integration is performed between the limits $\lambda_x = \mathcal{A}z$ and $\min[\lambda_x = \mathcal{A}z \exp 1/C_1, \lambda_x^{th}]$ (3.23) and (3.24). Similarly, $\overline{uu}_{ii,B}$ is obtained by integrating the energy spectra between the limits G and F for the spectral method, and between $\min[\lambda_x = \mathcal{A}z \exp 1/C_1, \lambda_x^{th}]$ and $\lambda_x/\Delta_E = 2\pi/F$, namely using the same low-frequency limit estimated through the spectral method.

Concerning the model for $\overline{uu}^+_{ii,A}$ derived from the AEH (2.9), in figure 14(*a*) the data seemingly shows a logarithmic vertical profile for both spectral and LCS methods, even though with significant differences in energy content and maximum height. The wall-attached component $\overline{uu}_{ii,A}$ is lower for the spectral method than for the LCS method, because, as reported in § 4.1, while the spectral limit P is slightly larger for the spectral method, the spectral limit G is significantly overestimated with respect to the LCS outcome (shorter spectral range between P and G for the spectral method), due to the overlap of the energy associated with larger coherent structures, e.g. VLSMs and superstructures, concealing the flat part of the premultiplied streamwise velocity energy spectra of region (ii_A). For the same reason, the component $\overline{uu}_{ii,B}$ is larger for the spectral method than for the LCS method. Similarly, z_{max} estimated from the spectral analysis is lower than that obtained from the LCS analysis being the limit $2\pi/G$ smaller than $\lambda_x^{th} \approx 4.5$ estimated through the LCS method, thus the intersection of the high-frequency limit of the spectral

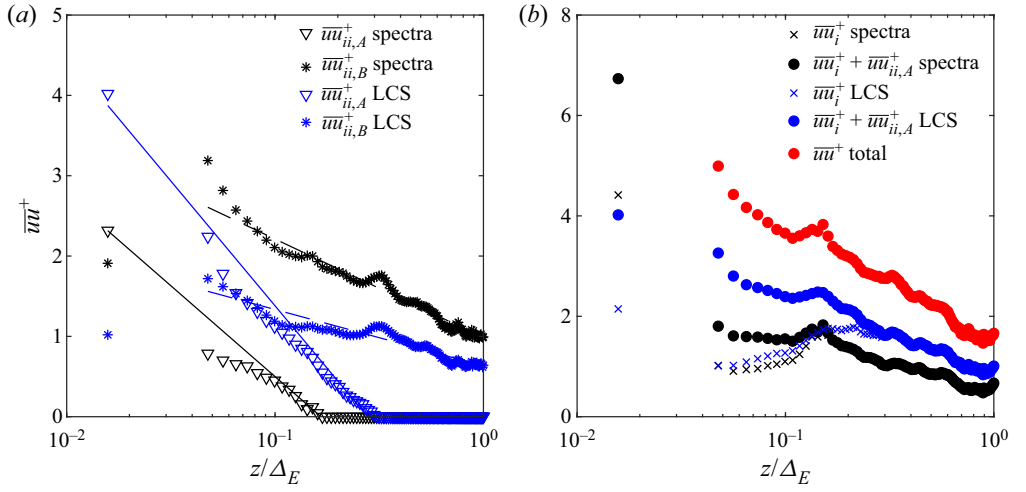

Figure 14. Vertical profiles of the streamwise turbulence intensity considering different eddy typologies and identification techniques. (*a*) Contributions over region (ii$_A$) and (ii$_B$) identified through the spectral method and the LCS. (*b*) Cumulative contributions to $\overline{uu}$.

region (ii$_A$) with the low-frequency limit occurs at higher wall-normal positions for the results obtained from the LCS.

The vertical profiles of $\overline{uu}^+_{ii,A}$ are fitted with the model based on the AEH in (2.9) to estimate the parameters A_1 and B_1, which are reported in table 3. It is noteworthy that the fitting has been limited to LiDAR gates with $z \geq 18$ m, which is the LiDAR range gate, to avoid possible underestimation of $\overline{uu}$ due to the LiDAR spatial averaging over the probe volume (see Appendix B). As shown in table 3, A_1 is generally estimated very close to 1, namely equal to 0.98 or 1.35 if estimated through the spectral or the LCS method, respectively. The former is very close to the recent estimate provided by Baars & Marusic (2020*b*) (0.975) where only the wall-attached-eddy contribution is considered. Thus, the spectral method seems to return the correct energy rate with height for the wall-attached-eddy component to the turbulence intensity, even though $\overline{uu}_{ii,A}$ can be underestimated. The values for B_1 are very close, namely -1.76 and -1.73 for the spectral and the LCS method, respectively. In Baars & Marusic (2020*b*), B_1 for $\overline{uu}^+_{ii,A}$ was estimated equal to -2.26.

The best fit of the experimental profiles of $\overline{uu}^+_{ii,A}$ with (2.9) is also performed for the vertical profiles obtained using the spectral limits proposed by Hwang (2015) and Hu *et al.* (2020), whose results are reported in table 3. The spectral boundaries of Hu *et al.* (2020) lead to a fitted value of A_1 comparable with that estimated by the authors (0.98 vs 1.0) while using the spectral limits proposed by Hwang (2015) leads to an estimate closer to the value obtained with the LCS method, i.e. $A_1 = 1.22$.

From (2.9), we can estimate the height where $\overline{uu}^+_{ii,A}$ becomes zero, i.e. $z_{max}/\Delta_E = \exp(B_1/A_1)$, which is reported in table 3 and compared against the previously reported values of z_{max} estimated independently from the streamwise velocity energy spectra or the LCS. A good agreement between z_{max}/Δ_E and $\exp(B_1/A_1)$ is generally observed for the different methods used for the detection of the energy contribution associated with wall-attached eddies, meaning that the selected streamwise energy is mainly limited to wall-attached-eddy contributions.

Reference	A_1		B_1			
	Region (ii$_A$)	Region (ii$_B$)	Region (ii$_A$)	Region (ii$_B$)	$\exp(B_1/A_1)$	$\frac{z_{max}}{\Delta_E}$
Present spectra	0.98 ± 0.06	0.53 ± 0.02	-1.76 ± 0.14	0.99 ± 0.02	0.17	0.17
Present LCS	1.35 ± 0.07	0.30 ± 0.02	-1.73 ± 0.13	0.63 ± 0.02	0.28	0.31
Hu *et al.* (2020)	1.05 ± 0.07	0.68 ± 0.04	-0.86 ± 0.10	1.07 ± 0.03	0.44	0.53
Hwang (2015)	1.22 ± 0.06	0.82 ± 0.04	-2.22 ± 0.15	1.21 ± 0.03	0.16	0.17
Baars & Marusic (2020*b*)	0.975	—	-2.26	—	0.10	—
Present global	1.11 ± 0.04		1.43 ± 0.05			

Table 3. Values of A_1 and B_1 of (2.9) calibrated with different methods and spectral regions. Uncertainty intervals refer to a 95 % confidence level.

Focusing on the energy associated with large coherent structures (star markers in figure 14*a*), a logarithmic wall-normal trend of $\overline{uu}^+_{ii,B}$ is seemingly observed throughout the vertical range probed by the LiDAR, as already noted in Hu *et al.* (2020), for both spectral and LCS methods. The results for B_1 and A_1 obtained by fitting $\overline{uu}^+_{ii,B}$ with (2.9) are reported in table 3 for all the considered spectral boundaries. First, A_1 for the wall-detached component is significantly smaller than for the wall-attached counterpart, specifically A_1 equal to 0.53 and 0.3 for the spectral and LCS methods, respectively. The parameter B_1 is positive, while for $\overline{uu}^+_{ii,A}$, it is generally negative and close to one.

It is noteworthy that the value of $\overline{uu}^+_{ii,B}$ measured by the sonic anemometer at $z/\Delta_E = 0.025$ is smaller than the maximum value of $\overline{uu}^+_{ii,B}$ measured by the LiDAR at $z/\Delta_E = 0.05$. This result is consistent with the work by Hu *et al.* (2020), where a maximum of $\overline{uu}^+_{ii,B}$ was observed at $z/\Delta_E = 0.045$. Unfortunately, more data between the minimum height probed by the LiDAR ($\approx$6 m) and the 2 m height of the sonic anemometer would be needed to draw more firm conclusions on the lower part of the vertical profile for $\overline{uu}^+_{ii,B}$.

Finally, a cumulative analysis of the streamwise turbulence intensity is reported in figure 14(*b*) for both spectral and LCS methods. The streamwise turbulence intensity associated with type-$\mathcal{C}$ eddies ($\overline{uu}^+_i$ with cross-symbols) is added to the energy associated with wall-attached eddies (blue and black circles), then the total streamwise turbulence intensity is achieved by adding the components associated with VLSMs.

5. Concluding remarks

A study of a high-Reynolds-number near-neutral ASL flow has been presented. The streamwise velocity was measured with a scanning Doppler pulsed wind LiDAR from a height of 6 m up to 143 m with a vertical resolution of approximately 1.08 m, and a sonic anemometer deployed at a 2 m height. The main goal of this study is to identify the energy contributions in the streamwise velocity associated with wall-attached eddies and larger coherent structures. Furthermore, the maximum height attained by wall-attached eddies has been estimated as well.

After quality control of the LiDAR data, assessment of their statistical stationarity and convergence, quantification of the spectral-gap frequency to filter out non-turbulent motions, i.e. mesoscales, and estimation of the outer scale of turbulence, Δ_E, the experimental data have mainly been interrogated through two different approaches: the

analysis of the energy spectra and the LCS of the streamwise velocity. The main findings of the present study are summarized as follows.

(i) Based on previous works about the LCS of the streamwise velocity induced by wall-attached eddies in turbulent boundary layers (e.g. Baars *et al.* 2017; Krug *et al.* 2019; Baars & Marusic 2020*a*) and the present results, an analytical model for the LCS inspired by the AEH (Townsend 1976) has been proposed. This model applies for wall-normal positions both below and above the considered reference height and for both wall-attached eddies and larger coherent structures. The model encompasses three parameters, i.e. the streamwise wavelength divided by the height for wall-attached eddies, i.e. their aspect ratio $\mathcal{AR}$, a parameter C_1, which represents the isolated-eddy contribution to the LCS for a given eddy population density, and an offset C_3. The parameter $\mathcal{AR}$, which is estimated to be about 14.3 from the present LiDAR data set, determines the small-wavelength boundary as a function of height of the spectral energy where contributions due to wall-attached eddies begin to build up, i.e. the spectral boundary between regions (i) and (ii$_A$). The parameter C_1 determines the spectral range over which these wall-attached-eddy contributions can be observed, i.e. $\log(\Delta\lambda_x/\Delta_E) = 1/C_1$, while the maximum height attained by wall-attached eddies is $\log(z_{max}/\Delta_E) = C_3/C_1$. It is noteworthy that the estimate of z_{max} from the LCS is analogous to that obtained from the AEH through the vertical law of the streamwise turbulence intensity, i.e. $\log(z_{max}/\Delta_E) = B_1/A_1$, where A_1 is the Townsend–Perry constant. For the LiDAR data set under investigation, it is found that $C_1 \approx 0.485$ and $C_3 \approx -0.56$, which leads to a maximum height for non-null streamwise turbulence intensity associated with wall-attached eddies of $z_{max}/\Delta_E \approx 0.31$. Finally, the proposed analytical LCS model enables the estimate of the spectral boundary, λ_x^{th}, between the energy associated with wall-attached eddies and that due to larger structures generated by their streamwise concatenation. For the present LiDAR data set, it is found that $\lambda_x^{th}/\Delta_E \approx 4.5$.

(ii) The analysis of the streamwise velocity energy spectra has enabled us to identify the k_x^{-1} region, allegedly associated with wall-attached eddies, for heights below $\approx 0.17\Delta_E$, which is a smaller estimate than that obtained from the LCS analysis ($0.31\Delta_E$). The high-wavenumber limit, P, is found to follow an inertial scaling, i.e. with an increasing wavenumber with increasing wall-normal position according to an aspect ratio of 10.8, which is smaller than the respective estimate from the LCS analysis ($\mathcal{AR} \approx 14.3$). In summary, the analysis of the streamwise velocity energy spectra for the detection of the spectral regions associated with different eddy typologies seems reasonable, although encompassing a high level of uncertainty in the estimates of the actual spectral limits of the various regions and the maximum height attained by wall-attached eddies. The main sources of this uncertainty are the empirical nature of the procedure and the presence of the energy associated with larger coherent structures, such as VLSMs and superstructures, obscuring the part of the premultiplied energy spectra with a roughly constant energy level. Nonetheless, even though the spectral range associated with wall-attached energy and, thus, the respective turbulence intensity are underestimated, the analysis of the streamwise velocity energy spectra enables good estimates of the Townsend–Perry constant.

(iii) The streamwise turbulence intensity associated with wall-attached eddies, $\overline{uu}_{ii,A}$, has been assessed against the AEH prediction. The parameter A_1 fitted from $\overline{uu}^+_{ii,A}$ leads to estimates of 0.98 and 1.35 for the spectral and LCS methods, respectively, which are in good agreement with the recent results presented in Baars & Marusic (2020*b*), thus confirming the scaling argument of Perry *et al.* (1986) for ASL flows.

The scattering in the estimates of A_1 might be caused by the different spectral limits between regions (ii_A) and (ii_B) identified with the spectral and LSC approach, which, in turn, leads to different values of integrated energy and, thus, wall-normal distributions. On one hand, the spectral-based underestimation of this boundary ($\lambda_x = 1.9\Delta_E$) leads to a downshift of the wall-normal profile of $\overline{uu}^+_{ii,A}$, yet it returns a more reliable estimate of A_1 (0.98) as it encompasses mainly type-$\mathcal{A}$ eddy contributions. On the other hand, the LCS-based estimate of this spectral boundary ($\lambda_x = 4.5\Delta_E$) leads to a cross-influence of larger coherent structures onto the wall-normal profile of $\overline{uu}^+_{ii,A}$, and, thus, to an overestimate of A_1. For region (ii_B), a logarithmic decay of integrated energy is observed, which seemingly confirms the scenario hypothesized by Hu *et al.* (2020) of a geometrically similar distribution of VLSMs.

In summary, this work has provided evidence that investigations of a near-neutral ASL flow with a scanning Doppler pulse wind LiDAR can open up research opportunities to investigate high-Reynolds-number turbulent boundary layers, upon the optimal design of the LiDAR scanning strategy and post-processing of the generated observations. In this work, the use of the LCS has enabled the identification of the energy components either coherent or incoherent with the ground, their spectral limits with height and the maximum height attained by wall-attached eddies. However, this current LCS approach shows symptoms of cross-contamination on the wall-attached energy contribution with those generated by type-$\mathcal{C}$ and type-$\mathcal{B}$ eddies, which might affect, for instance, the estimate of the Townsend–Perry constant. Finally, other data-driven approaches, coupled with the methods tested for this work, might provide more detailed and accurate analyses of the organization and dynamics of coherent structures in turbulent boundary layers, which might be the focus of future investigations.

Acknowledgments. M. Guala is acknowledged for providing literature data reported in figures 3 and 4.

Funding. This research has been funded by the National Science Foundation, Fluid Dynamics Program, award no. 1705837, and the NSF CAREER program, award no. 2046160, Program Manager Ron Joslin.

Declaration of interests. The authors report no conflict of interest.

Author ORCIDs.
Matteo Puccioni https://orcid.org/0000-0002-0764-9430;
Giacomo Valerio Iungo https://orcid.org/0000-0002-0990-8133.

Appendix A. Evaluation of the spectral gap and outer scale of turbulence

A challenge to investigating atmospheric turbulent flows is represented by the coexistence of turbulent scales of motion and background large-wavelength flow fluctuations affecting the entire boundary layer height, which are associated with the mesoscale flow component (e.g. Draxl *et al.* 2021). Although the non-turbulent mesoscale velocity fluctuations are expected to occur with larger wavelengths than those associated with turbulence, a systematic method for mesoscale-turbulence separation is still elusive (Högström *et al.* 2002; Metzger *et al.* 2007). The streamwise velocity energy spectrum typically presents a local minimum at the interface between turbulence and mesoscales, which is referred to as the 'spectral gap' (Van der Hoven 1957; Panofsky 1969; Högström *et al.* 2002; Wyngaard 2004; Metzger *et al.* 2007; Guala *et al.* 2011; Larsén *et al.* 2013, 2016), while the co-spectrum of the turbulent momentum flux, $\overline{uw}$, becomes negligible for frequencies lower than the spectral-gap frequency (Metzger *et al.* 2007).

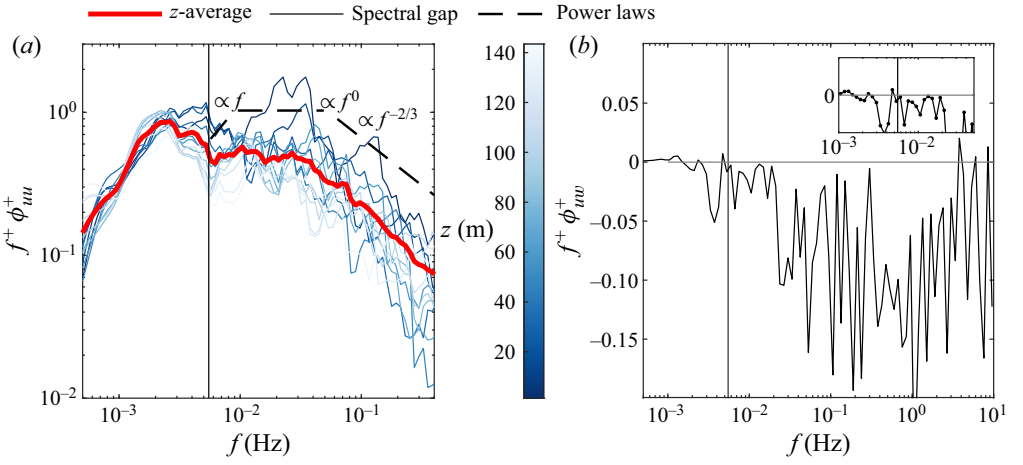

Figure 15. Detection of the spectral gap. (*a*) Premultiplied streamwise velocity energy spectra of the LiDAR data (the vertically averaged energy spectrum is reported with a red line). (*b*) Co-spectrum of the vertical turbulent momentum flux measured from the 'PA2' sonic anemometer.

For this work, the premultiplied streamwise velocity energy spectra obtained from the wind LiDAR measurements, and the co-spectrum of the vertical turbulent momentum flux measured from the sonic anemometer 'PA2' (figure 1*a*) are analysed. The energy spectra reported in figure 15(*a*) versus frequency, f, are calculated at each height sampled with the LiDAR through the Welch spectrogram (Welch 1967) using a window length of 0.0003 Hz and 10 % overlapping between consecutive sub-periods. The energy spectra are evaluated over 100 frequencies logarithmically spaced between 10^{-4} and 0.5 Hz (the Nyquist frequency), which are then smoothed through a moving-average algorithm with a spectral stencil of $f_i \pm 0.35 f_i$ for a generic frequency f_i (Baars & Marusic 2020*a*). The wall-normal average between all the spectra is then calculated and reported in figure 15(*a*) with a red line. The premultiplied energy spectra of the streamwise velocity indicate the spectral gap at a frequency of about 0.0055 Hz (i.e. period of 181.8 s), which is very close to the value reported in Metzger *et al.* (2007) (0.005 Hz) for a neutrally stratified flow probed at the SLTEST facility through a vertical array of sonic anemometers, and it is in good agreement with the detrending period of 198 s (corresponding to 0.00505 Hz) and 180 s (corresponding to 0.0055 Hz) used in Guala *et al.* (2011) and Hutchins *et al.* (2012), respectively, to remove mesoscale contributions from the velocity turbulence statistics.

The estimate for the spectral-gap frequency is also supported by the analysis of the co-spectrum of the vertical momentum flux measured through the PA2 sonic anemometer (figure 15*b*), which is obtained through the Welch spectrogram algorithm for 500 frequencies logarithmically spaced between 10^{-4} and 10 Hz (Nyquist value), and using a window length of 0.0003 Hz with a 10 % overlapping period. The co-spectrum is bin averaged over 100 non-overlapping bins to highlight the zero-crossing region at low frequencies, which is approximately located at 0.0055 Hz. The latter is practically equal to the spectral-gap frequency quantified through the LiDAR data.

The quantification of the spectral-gap frequency is also instrumental for the estimate of the outer scale of turbulence, Δ_E, which is assumed as the wall-normal position where the turbulence intensity achieves a minimum value (Gryning *et al.* 2014, 2016). For each height, the Weibull probability density function of the streamwise velocity is generated

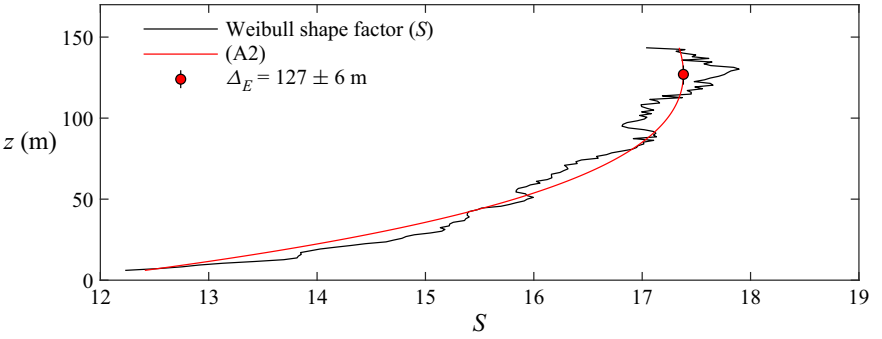

Figure 16. Vertical profile of the Weibull shape parameter, S, estimated from the LiDAR velocity signals (black line) and fitted through the model of (A2) (red line).

(Gryning *et al.* 2016),

$$f_u(u) = \frac{S}{B}\left(\frac{u}{B}\right)^{S-1} \exp\left[-\left(\frac{u}{B}\right)^{S}\right], \tag{A1}$$

where S and B represent the shape and scale parameters, respectively, and u is the zero-mean velocity fluctuation. The minimum of the turbulence intensity is identified from the maximum of the shape parameter, S, throughout the vertical range probed by the LiDAR (Gryning *et al.* 2016). Subsequently, the vertical profile of S is parametrized through the model proposed by Gryning *et al.* (2014, 2016) for heights lower than Δ_E,

$$S(z;\, \Delta_E, c) = S_{min} + c\frac{z - z_{min}}{\Delta_E - z_{min}} \exp\left(-\frac{z - z_{min}}{\Delta_E - z_{min}}\right), \tag{A2}$$

where S_{min} is the shape parameter associated with the lowest height probed, z_{min}, which is equal to 6 m for the data set under investigation. It should be noted that in Gryning *et al.* (2014) a second term is added to (A2), which refers to the shape parameter distribution above Δ_E. The outer scale of turbulence and the dimensionless parameter c of (A2) are obtained from the least-squares fitting of the vertical profile of S estimated from the LiDAR data. It is obtained that $\Delta_E = 127$ m $\pm$ 6 m with a 95 % confidence level, as visualized in figure 16.

Appendix B. Spectral correction of the LiDAR velocity measurements

Wind velocity measurements performed with a Doppler wind LiDAR entail an averaging process over each measurement volume, which is mainly affected by the probe length, l, of each laser pulse, and the spatial distribution of the energy within the laser pulse. The radial velocity recorded at a radial distance r can be modelled as the convolution between the true radial speed $\tilde{V}_r(r, t)$, namely the wind velocity component along the direction of the LiDAR laser beam, and a weighting function $\omega(r)$ representing the energy distribution along the laser pulse (Frehlich *et al.* 1998; Frehlich & Cornman 2002; Mann *et al.* 2009; Cheynet *et al.* 2017; Puccioni & Iungo 2021),

$$V_r(r, t) = \int_{-l/2}^{l/2} \tilde{V}_r(r + x', t)\omega(x')\, \mathrm{d}x'. \tag{B1}$$

For the LiDAR unit used for this experiment, $l = 18$ m and $\omega = 0$ outside of the range gate. The convolution in the physical domain corresponds to a product in the spectral domain

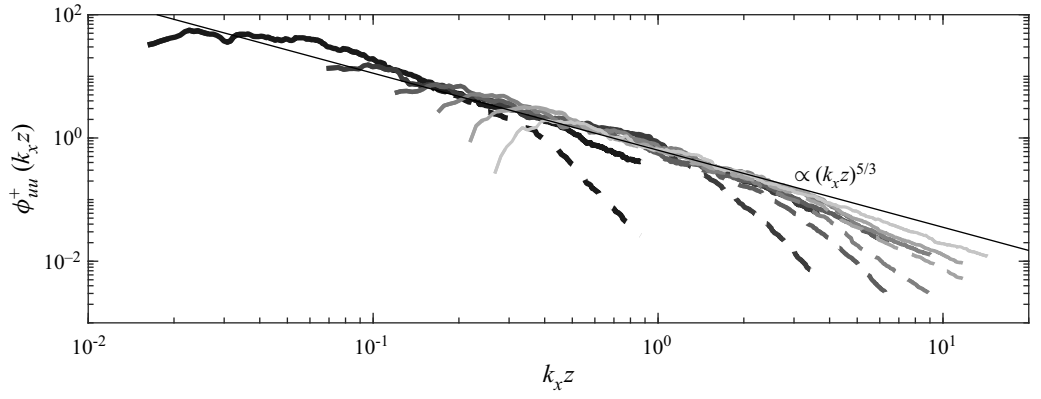

Figure 17. Correction of the streamwise velocity energy spectra obtained from the LiDAR measurements at six different wall-normal positions equally spaced between 6 and 121 m, respectively. Lines become darker with increasing height. Continuous lines represent corrected spectra, while dashed lines report raw spectra.

between the true streamwise velocity spectrum ($\tilde{\phi}_{uu}(k_x)$) and the squared modulus of the Fourier transform of ω (said $\Omega(k_x)$) (Mann *et al.* 2009; Puccioni & Iungo 2021), such as the energy spectrum of the measured velocity signal can be estimated as

$$\phi_{uu}(k_x) = |\Omega(k_x)|^2 \tilde{\phi}_{uu}(k_x). \tag{B2}$$

Therefore, if $|\Omega(k_x)|^2$ across frequencies was known, the low-pass filtering effect due to the LiDAR spatial averaging could be reverted to correct the streamwise velocity energy spectra and, thus, turbulence intensity. In this work this correction is performed by using the method proposed in Puccioni & Iungo (2021), which does not require any input related to the technical specifications of the used LiDAR system, such as the energy distribution over the laser pulse and LiDAR probe length, while it is completely data driven. Specifically, the spectral model of Kaimal *et al.* (1972) for a neutrally stratified ASL flow is firstly calibrated on the low-wavenumber portion of each experimental spectrum; then, the missing energy portion is quantified through the ratio between the LiDAR and the Kaimal *et al.* (1972) spectra and fitted with a low-pass filter model. Finally, the latter is used to revert the range-gate averaging effect onto the original spectrum.

The results of the correction procedure are reported in figure 17 for LiDAR velocity measurements collected at six different range gates, i.e. wall-normal positions. It is observed that, after the spectral correction, the expected $k_x^{-5/3}$ slope is roughly recovered for all the velocity signals, together with a good overlapping on the same power law when the spectra are reported as a function of the inertia-scaled wavenumber, $k_x z$ (Perry *et al.* 1986).

For the lowest part of the ASL ($z < l$), it should be noted that the present correction method still underestimates the spectral energy, as the k_x^{-1} region is also affected by the LiDAR spatial averaging. Other spectral correction procedures were tested (Mann *et al.* 2009; Cheynet *et al.* 2017), while the data-driven method of Puccioni & Iungo (2021) provided the largest variance recovery.

Appendix C. Smoothing of the LCS

The parameters for the Welch spectral estimator (Welch 1967), namely window length and overlapping, used for the calculation of the LCS are firstly determined by leveraging a

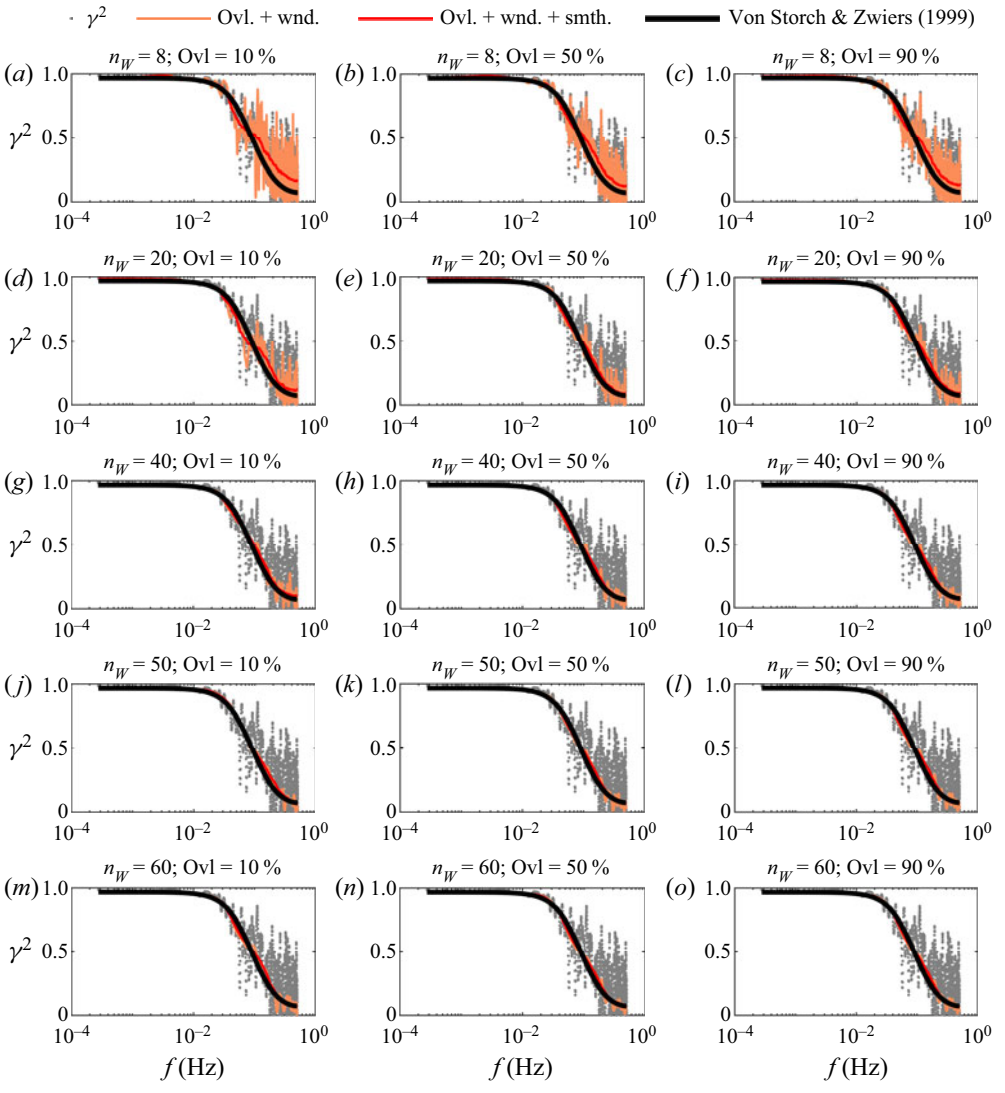

Figure 18. Sensitivity of the LCS to the windowing and overlapping parameters for a synthetic autoregressive case. Grey dots report the LCS without smoothing, the orange lines depict γ^2 calculated with the Welch (1967) periodogram with the indicated windowing and smoothing parameters, the red lines reports the result after the smoothing procedure and the black lines are the theoretical distribution of Von Storch & Zwiers (1999).

synthetic first-order autoregressive model, q_n, defined as (Von Storch & Zwiers 1999)

$$q_n = \begin{cases} e_n & \text{as } n = 1, \\ \alpha q_{n-1} + e_n & \text{as } n > 1, \end{cases} \tag{C1}$$

where e_n is a white-noise Gaussian process with variance σ_e^2, $0 < \alpha < 1$ and $n = 1, \ldots, M$. From (C1) a second synthetic signal can be defined as

$$s_n = \beta q_n + \tilde{e}_n, \tag{C2}$$

where $\tilde{e}_n$ is another white-noise Gaussian process with variance $\tilde{\sigma}_e^2$, and $0 < \beta < 1$. From the definition of auto- and cross-spectra, it is possible to show that the coherence between

q and s is given by

$$\gamma^2(q, s; f) = \frac{\beta^2 \phi_{qq}(f)}{\beta^2 \phi_{qq}(f) + \tilde{\sigma}_e^2}, \tag{C3}$$

where f is the frequency and

$$\phi_{qq}(f) = \frac{\sigma_e^2}{1 + \alpha^2 - 2\alpha \cos(2\pi f)}. \tag{C4}$$

Thus, leveraging these two related autoregressive signals q_n and s_n, a theoretical reference for the LCS is available against which the numerical algorithm for the evaluation of the LCS from the two signals can be assessed.

As previously mentioned, the coherence for two time series is calculated by means of the Welch (1967) algorithm; the ensemble averaging operation in (3.15) is simulated by dividing the entire signals into a certain number of sub-windows, n_W, with a certain overlapping percentage. Successively, a moving average with stencil $f_n \pm 0.35 f_n (n = 1, \ldots, M)$ is performed to smooth the LCS (Baars *et al.* 2017; Baars & Marusic 2020*a*).

The algorithm for the calculation of the LCS between the discrete signals of (C1) and (C2) is tested, then the results are compared against the analytical LCS reported in (C3). The results obtained from this sensitivity study are reported in figure 18 using $\alpha = 0.9$, $\beta = 0.3$ for a signal with $M = 3600$ samples simulated with a sampling frequency of 1 Hz. A close agreement between the numerical results and the analytical prediction is obtained for the case with $n_W = 20$ and 90 % overlapping (figure 18*f*), which are the parameters used for the present work.

References

Adrian, R.J. 2007 Hairpin vortex organization in wall turbulence. *Phys. Fluids* **19** (4), 041301.

Baars, W.J., Hutchins, N. & Marusic, I. 2017 Self-similarity of wall-attached turbulence in boundary layers. *J. Fluid Mech.* **823**, R2.

Baars, W.J. & Marusic, I. 2020*a* Data-driven decomposition of the streamwise turbulence kinetic energy in boundary layers. Part 1. Energy spectra. *J. Fluid Mech.* **882**, A25.

Baars, W.J. & Marusic, I. 2020*b* Data-driven decomposition of the streamwise turbulence kinetic energy in boundary layers. Part 2. Integrated energy and A_1. *J. Fluid Mech.* **882**, A26.

Baidya, R., Philip, J., Hutchins, N., Monty, J.P. & Marusic, I. 2017 Distance-from-the-wall scaling of turbulent motions in wall-bounded flows. *Phys. Fluids* **29** (2), 020712.

Balakumar, B.J. & Adrian, R.J. 2007 Large- and very-large-scale motions in channel and boundary-layer flows. *Phil. Trans. R. Soc.* A **365** (1852), 665–681.

Barlow, J.F. 2014 Progress in observing and modelling the urban boundary layer. *Urban Clim.* **10**, 216–240.

Beck, H. & Kühn, M. 2017 Dynamic data filtering of long-range Doppler LiDAR wind speed measurements. *Remote Sens.* **9** (6), 561.

Bendat, J.S. & Piersol, A.G. 1986 *Random Data*. John Wiley & Sons.

Bernardini, M., Pirozzoli, S. & Orlandi, P. 2014 Velocity statistics in turbulent channel flow up to $Re_\tau = 4000$. *J. Fluid Mech.* **742**, 171–191.

Businger, J.A., Wyngaard, J.C., Izumi, Y. & Bradley, E.F. 1971 Flux-profile relationships in the atmospheric surface layer. *J. Atmos. Sci.* **28**, 181–189.

Calaf, M., Hultmark, M., Oldroyd, H.J., Simeonov, V. & Parlange, M.B. 2013 Coherent structures and the k^{-1} spectral behaviour. *Phys. Fluids* **25** (12), 125107.

Carbajo Fuertes, F., Iungo, G.V. & Porté-Agel, F. 2014 3D turbulence measurements using three synchronous wind lidars: validation against sonic anemometry. *J. Atmos. Ocean. Technol.* **31** (7), 1549–1556.

Cheynet, E., Jakobsen, J.B., Snæbjörnsson, J., Mann, J., Courtney, M.S., Lea, G. & Svardal, B. 2017 Measurements of surface-layer turbulence in a wide Norwegian fjord using synchronized long-range Doppler wind lidars. *Remote Sens.* **9** (10), 1–26.

CLARKE, R.H., DYER, A.J., BROOK, R.R., REID, D.G. & TROUP, A.J. 1971 The Wangara experiment: boundary layer data. Technical Paper 19. CSIRO Australia.

DAVIDSON, P.A. & KROGSTAD, P.-Å. 2009 A simple model for the streamwise fluctuations in the log-law region of a boundary layer. *Phys. Fluids* **21** (5), 055105.

DE SILVA, C.M., HUTCHINS, N. & MARUSIC, I. 2015 Uniform momentum zones in turbulent boundary layers. *J. Fluid Mech.* **786**, 309–331.

DEBNATH, M., IUNGO, G.V., ASHTON, R., BREWER, W.A., CHOUKULKAR, A., DELGADO, R., LUNDQUIST, J.K., SHAW, W.J., WILCZAK, J.M. & WOLFE, D. 2017*a* Vertical profiles of the 3-D wind velocity retrieved from multiple wind lidars performing triple range-height-indicator scans. *Atmos. Meas. Tech.* **10** (2), 431–444.

DEBNATH, M., IUNGO, G.V., BREWER, W.A., CHOUKULKAR, A., DELGADO, R., GUNTER, S., LUNDQUIST, J.K., SCHROEDER, J.L., WILCZAK, J.M. & WOLFE, D. 2017*b* Assessment of virtual towers performed with scanning wind lidars and Ka-band radars during the XPIA experiment. *Atmos. Meas. Tech.* **10** (3), 1215–1227.

D'ERRICO, J. 2004 Inpaint nans. MATLAB Central File Exchange.

DRAXL, C., ALLAERTS, D., QUON, E. & CHURCHFIELD, M. 2021 Coupling mesoscale budget components to large-eddy simulations for wind-energy applications. *Boundary-Layer Meteorol.* **179** (1), 73–98.

DROBINSKI, P., CARLOTTI, P., REDELSPERGER, J.-L., BANTA, R.M., MASSON, V. & NEWSOM, R.K. 2007 Numerical and experimental investigation of the neutral atmospheric surface layer. *J. Atmos. Sci.* **64** (1), 137–156.

EL-ASHA, S., ZHAN, L. & IUNGO, G.V. 2017 Quantification of power losses due to wind turbine wake interactions through SCADA, meteorological and wind LiDAR data. *Wind Energy* **20** (11), 1823–1839.

FOKEN, T., GÖOCKEDE, M., MAUDER, M., MAHRT, L., AMIRO, B. & MUNGER, W. 2004 Post-field data quality control. In *Handbook of Micrometeorology* (ed. X. Lee, W. Massmann & B. Law), pp. 181–208. Springer.

FOKEN, T. & WICHURA, B. 1996 Tools for quality assessment of surface-based flux measurements. *Agric. Forest Meteorol.* **78** (1–2), 83–105.

FREHLICH, R. 1997 Effects of wind turbulence on coherent Doppler lidar performance. *J. Atmos. Ocean. Technol.* **14** (1), 54–75.

FREHLICH, R. & CORNMAN, L. 2002 Estimating spatial velocity statistics with coherent Doppler lidar. *J. Atmos. Ocean. Technol.* **19** (3), 355–366.

FREHLICH, R., HANNON, S.M. & HENDERSON, S.W. 1998 Coherent Doppler lidar measurements of wind field statistics. *Boundary-Layer Meteorol.* **86** (2), 233–256.

GRYNING, S.E., BATCHVAROVA, E., BRÜMMER, B., JØRGENSEN, H.E. & LARSÉN, S.E. 2007 On the extension of the wind profile over homogeneous terrain beyond the surface boundary layer. *Boundary-Layer Meteorol.* **124** (2), 251–268.

GRYNING, S.E., BATCHVAROVA, E., FLOORS, R., PEÑA, A., BRÜMMER, B., HAHMANN, A.N. & MIKKELSEN, T. 2014 Long-term profiles of wind and Weibull distribution parameters up to 600 m in a rural coastal and an inland suburban area. *Boundary-Layer Meteorol.* **150** (2), 167–184.

GRYNING, S.E. & FLOORS, R. 2019 Carrier-to-noise-threshold filtering on off-shore wind lidar measurements. *Sensors* **19** (3), 592.

GRYNING, S.E., FLOORS, R., PEÑA, A., BATCHVAROVA, E. & BRÜMMER, B. 2016 Weibull wind-speed distribution parameters derived from a combination of wind-lidar and tall-mast measurements over land, coastal and marine sites. *Boundary-Layer Meteorol.* **159** (2), 329–348.

GUALA, M., HOMMEMA, S.E. & ADRIAN, R.J. 2006 Large-scale and very-large-scale motions in turbulent pipe flow. *J. Fluid Mech.* **554**, 521–542.

GUALA, M., METZGER, M. & MCKEON, B.J. 2011 Interactions within the turbulent boundary layer at high Reynolds number. *J. Fluid Mech.* **666**, 573–604.

HEISEL, M., DASARI, T., LIU, Y., HONG, J., COLETTI, F. & GUALA, M. 2018 The spatial structure of the logarithmic region in very-high-Reynolds-number rough wall turbulent boundary layers. *J. Fluid Mech.* **857**, 704–747.

HÖGSTRÖM, U. 1990 Analysis of turbulence structure in the surface layer with a modified similarity formulation for near neutral conditions. *J. Atmos. Sci.* **47** (16), 1949–1972.

HÖGSTRÖM, U. 1992 Further evidence of 'inactive' turbulence in the near neutral atmospheric surface layer. In *Proceedings, 10th Symposium of Turbulence and Diffusion*, vol. 29, pp. 188–191. American Meteorological Society.

HÖGSTRÖM, U., HUNT, J.C.R. & SMEDMAN, A.S. 2002 Theory and measurements for turbulence spectra and variances in the atmospheric neutral surface layer. *Boundary-Layer Meteorol.* **103** (1), 101–124.

HØJSTRUP, J. 1993 A statistical data screening procedure. *Meas. Sci. Technol.* **4** (2), 153.

HOMMEMA, S.E. & ADRIAN, R.J. 2003 Packet structure of surface eddies in the atmospheric boundary layer. *Boundary-Layer Meteorol.* **106** (1), 147–170.

HU, R., YANG, X.I.A. & ZHENG, X. 2020 Wall-attached and wall-detached eddies in wall-bounded turbulent flows. *J. Fluid Mech.* **885**, A30–24.

HUANG, K.Y., BRUNNER, C.E., FU, M.K., KOKMANIAN, K., MORRISON, T.J., PERELET, A.O., CALAF, M., PARDYJAK, E. & HULTMARK, M. 2021 Investigation of the atmospheric surface layer using a novel high-resolution sensor array. *Exp. Fluids* **62** (4), 1–13.

HUNT, J.C.R. & MORRISON, J.F. 2000 Eddy structure in turbulent boundary layers. *Eur. J. Mech.* B*/Fluids* **19** (5), 673–694.

HUTCHINS, N., CHAUHAN, K., MARUSIC, I., MONTY, J. & KLEWICKI, J. 2012 Towards reconciling the large-scale structure of turbulent boundary layers in the atmosphere and laboratory. *Boundary-Layer Meteorol.* **145** (2), 273–306.

HUTCHINS, N. & MARUSIC, I. 2007 Evidence of very long meandering features in the logarithmic region of turbulent boundary layers. *J. Fluid Mech.* **579**, 1–28.

HWANG, J. & SUNG, H.J. 2018 Wall-attached structures of velocity fluctuations in a turbulent boundary layer. *J. Fluid Mech.* **856**, 958–983.

HWANG, Y. 2015 Statistical structure of self-sustaining attached eddies in turbulent channel flow. *J. Fluid Mech.* **767**, 254–289.

IUNGO, G.V., WU, Y.-T. & PORTÉ-AGEL, F. 2013 Field measurements of wind turbine wakes with lidars. *J. Atmos. Ocean. Technol.* **30** (2), 274–287.

JIMÉNEZ, J. 2004 Turbulent flows over rough walls. *Annu. Rev. Fluid Mech.* **36**, 173–196.

JIMÉNEZ, J. 2018 Coherent structures in wall-bounded turbulence. *J. Fluid Mech.* **842**, P1.

JIMÉNEZ, J. & MOSER, R.D. 2007 What are we learning from simulating wall turbulence? *Phil. Trans. R. Soc.* A **365** (1852), 715–732.

KAIMAL, J.C., WYNGAARD, J.C., IZUMI, Y. & COTÉ, O.R. 1972 Spectral characteristics of surface-layer turbulence. *Q. J. R. Meteorol. Soc.* **98** (417), 563–589.

KIM, K.C. & ADRIAN, R.J. 1999 Very large-scale motion in the outer layer. *Phys. Fluids* **11** (2), 417–422.

KLEWICKI, J.C. 2021 Laboratory realization of an asymptotic wall flow. *J. Fluid Mech.* **918**, 1–4.

KLEWICKI, J.C., METZGER, M., KELNER, E. & THURLOW, E. 1995 Viscous sublayer flow visualizations at $R_\theta = 150\,000$. *Phys. Fluids* **7**, 857–863.

KLINE, S.J., REYNOLDS, W.C., SCHRAUB, F.A. & RUNSTADLER, P.W. 1967 The structure of turbulent boundary layers. *J. Fluid Mech.* **30** (4), 741–773.

KRUG, D., BAARS, W.J., HUTCHINS, N. & MARUSIC, I. 2019 Vertical coherence of turbulence in the atmospheric surface layer: connecting the hypotheses of Townsend and Davenport. *Boundary-Layer Meteorol.* **172** (2), 199–214.

KUNKEL, G.J. & MARUSIC, I. 2006 Study of the near-wall-turbulent region of the high-Reynolds-number boundary layer using an atmospheric flow. *J. Fluid Mech.* **548**, 375–402.

LARSÉN, X.G., LARSEN, S.E. & PETERSEN, E.L. 2016 Full-scale spectrum of boundary-layer winds. *Boundary-Layer Meteorol.* **159** (2), 349–371.

LARSÉN, X.G., VINCENT, C. & LARSEN, S.E. 2013 Spectral structure of mesoscale winds over the water. *Q. J. R. Meteorol. Soc.* **139** (672), 685–700.

LEE, M. & MOSER, R.D. 2015 Direct numerical simulation of turbulent channel flow up to $Re_\tau \approx 5200$. *J. Fluid Mech.* **774**, 395–415.

LEE, M. & MOSER, R.D. 2019 Spectral analysis of the budget equation in turbulent channel flows at high Reynolds number. *J. Fluid Mech.* **860**, 886–938.

LETIZIA, S., ZHAN, L. & IUNGO, G.V. 2021*a* LiSBOA (LiDAR statistical barnes objective analysis) for optimal design of Lidar scans and retrieval of wind statistics. Part 1. Theoretical framework. *Atmos. Meas. Tech.* **14** (3), 2065–2093.

LETIZIA, S., ZHAN, L. & IUNGO, G.V. 2021*b* LiSBOA (LiDAR statistical barnes objective analysis) for optimal design of Lidar scans and retrieval of wind statistics. Part 2. Applications to liDAR measurements of wind turbine wakes. *Atmos. Meas. Tech.* **14** (3), 2095–2113.

LI, X., WANG, G. & ZHENG, X. 2021 Turbulent/synoptic separation and coherent structures in the atmospheric surface layer for a range of surface roughness. *Boundary-Layer Meteorol.* **182**, 75–93.

LIGRANI, P.M. & MOFFAT, R.J. 1986 Structure of transitionally rough and fully rough turbulent boundary layers. *J. Fluid Mech.* **162**, 69–98.

LIU, H.Y., BO, T.L. & LIANG, Y.R. 2017 The variation of large-scale structure inclination angles in high Reynolds number atmospheric surface layers. *Phys. Fluids* **29** (3), 035104.

LIU, H.Y., WANG, G. & ZHENG, X. 2019 Amplitude modulation between multi-scale turbulent motions in high-Reynolds-number atmospheric surface layers. *J. Fluid Mech.* **861**, 585–607.

LUNDQUIST, J.K., *et al.* 2017 Assessing state-of-the-art capabilities for probing the atmospheric boundary layer: the XPIA field campaign. *Bull. Am. Meteorol. Soc.* **98**, 289–314.

MANN, J., CARIOU, J.P., COURTNEY, M.S., PARMENTIER, R., MIKKELSEN, T., WAGNER, R., LINDELÖW, P., SJÖHOLM, M. & ENEVOLDSEN, K. 2009 Comparison of 3D turbulence measurements using three staring wind lidars and a sonic anemometer. *Meteorol. Z.* **18** (2), 135–140.

MARUSIC, I., MCKEON, B.J., MONKEWITZ, P.A., NAGIB, H.M., SMITS, A.J. & SREENIVASAN, K.R. 2010 Wall-bounded turbulent flows at high Reynolds numbers: recent advances and key issues. *Phys. Fluids* **22** (6), 065103.

MARUSIC, I. & MONTY, J.P. 2018 Attached eddy model of wall turbulence. *Annu. Rev. Fluid Mech.* **51** (1), 49–74.

MARUSIC, I., MONTY, J., HULTMARK, M. & SMITS, A.J. 2013 On the logarithmic region in wall turbulence. *J. Fluid Mech.* **716** (2), R3–1–R3–11.

MARUSIC, I. & PERRY, A.E. 1995 A wall-wake model for the turbulence structure of boundary layers. Part 2. Further experimental support. *J. Fluid Mech.* **298**, 389–407.

MATHIS, R., HUTCHINS, N. & MARUSIC, I. 2009 Large-scale amplitude modulation of the small-scale structures in turbulent boundary layers. *J. Fluid Mech.* **628** (2009), 311–337.

MENEVEAU, C. & MARUSIC, I. 2013 Generalized logarithmic law for high-order moments in turbulent boundary layers. *J. Fluid Mech.* **719**, 1–11.

METZGER, M., MCKEON, B.J. & HOLMES, H. 2007 The near-neutral atmospheric surface layer: turbulence and non-stationarity. *Phil. Trans. R. Soc.* A **365** (1852), 859–876.

MIKKELSEN, T., COURTNEY, M., ANTONIOU, I. & MANN, J. 2008 Wind scanner: a full-scale laser facility for wind and turbulence measurements around large wind turbines. In *Conference Proceedings (online)*. European Wind Energy Association (EWEA).

MONIN, A.S. & OBUKHOV, A.M. 1954 Basic laws of turbulent mixing in the surface layer of the atmosphere. *Contrib. Geophys. Inst. Acad. Sci. USSR* **24** (151), 163–187.

MORRILL-WINTER, C., SQUIRE, D.T., KLEWICKI, J.C., HUTCHINS, N., SCHULTZ, M.P. & MARUSIC, I 2017 Reynolds number and roughness effects on turbulent stresses in sandpaper roughness boundary layers. *Phys. Rev. Fluids* **2** (5), 054608.

MORRISON, J.F. 2007 The interaction between inner and outer regions of turbulent wall-bounded flow. *Phil. Trans. R. Soc.* A **365** (1852), 683–698.

MORRISON, J.F., JIANG, W., MCKEON, B.J. & SMITS, A.J. 2002 Reynolds number dependence of streamwise velocity spectra in turbulent pipe flow. *Phys. Rev. Lett.* **88** (21), 214501.

MOURI, H., MORINAGA, T. & HAGINOYA, S. 2019 Unlikely existence of k_x^{-1} spectral law in wall turbulence: an observation of the atmospheric surface layer. *Phys. Fluids* **31** (3), 035103.

NELSON, C.W., HATI, A. & HOWE, D.A. 2013 Phase inversion and collapse of cross-spectral function. *Electron. Lett.* **49** (25), 1640–1641.

NICKELS, T.B., MARUSIC, I., HAFEZ, S. & CHONG, M.S. 2005 Evidence of the k^{-1} law in a high-Reynolds-number turbulent boundary layer. *Phys. Rev. Lett.* **95** (7), 074501.

ÖNDER, A. & MEYERS, J. 2018 On the interaction of very-large-scale motions in a neutral atmospheric boundary layer with a row of wind turbines. *J. Fluid Mech.* **841**, 1040–1072.

PANOFSKY, H.A. 1969 Spectra of atmospheric variables in the boundary layer. *Radio Sci.* **4** (12), 1101–1109.

PERRY, A.E. & ABELL, C.J. 1975 Scaling laws for pipe-flow turbulence. *J. Fluid Mech.* **67** (2), 257–271.

PERRY, A.E. & ABELL, C.J. 1977 Asymptotic similarity of turbulence structures in smooth-and rough-walled pipes. *J. Fluid Mech.* **79** (4), 785–799.

PERRY, A.E. & CHONG, M.S. 1982 On the mechanism of wall turbulence. *J. Fluid Mech.* **119**, 173–217.

PERRY, A.E., HENBEST, S. & CHONG, M.S. 1986 A theoretical and experimental study of wall turbulence. *J. Fluid Mech.* **165**, 163–199.

PERRY, A.E. & MARUSIC, I. 1995 A wall-wake model for the turbulence structure of boundary layers. Part 1. Extension of the attached eddy hypothesis. *J. Fluid Mech.* **298**, 361–388.

PICARD, A., DAVIS, R.S., GLÄSER, M. & FUJII, K. 2008 Revised formula for the density of moist air (CIPM-2007). *Metrologia* **45** (2), 149.

PUCCIONI, M. & IUNGO, G.V. 2021 Spectral correction of turbulent energy damping on wind LiDAR measurements due to range-gate averaging. *Atmos. Meas. Tech.* **14**, 1457–1474.

RECHE, I., D'ORTA, G., MLADENOV, N., WINGET, D.M. & SUTTLE, C.A. 2018 Deposition rates of viruses and bacteria above the atmospheric boundary layer. *ISME J.* **12** (4), 1154–1162.

ROSENBERG, B.J., HULTMARK, M., VALLIKIVI, M., BAILEY, S.C.C. & SMITS, A.J. 2013 Turbulence spectra in smooth- and rough-wall pipe flow at extreme Reynolds numbers. *J. Fluid Mech.* **731**, 46–63.

ROSSBY, C.G. & MONTGOMERY, R.B. 1935 The layer of frictional influence in wind and ocean currents. *Pap. Phys. Oceanogr. Meteorol.* **3** (3), 101.

SALESKY, S.T. & ANDERSON, W. 2020 Coherent structures modulate atmospheric surface layer flux-gradient relationships. *Phys. Rev. Lett.* **125** (12), 124501.

SATHE, A. & MANN, J. 2013 A review of turbulence measurements using ground-based wind lidars. *Atmos. Meas. Tech.* **6** (11), 3147–3167.

SCHULTZ, M.P. & FLACK, K.A. 2007 The rough-wall turbulent boundary layer from the hydraulically smooth to the fully rough regime. *J. Fluid Mech.* **580**, 381–405.

SMITS, A.J., MCKEON, B.J. & MARUSIC, I. 2011 High–Reynolds number wall turbulence. *Annu. Rev. Fluid Mech.* **43** (43), 353–375.

SQUIRE, D.T., MORRILL-WINTER, C., HUTCHINS, N., SCHULTZ, M.P., KLEWICKI, J.C. & MARUSIC, I. 2016 Comparison of turbulent boundary layers over smooth and rough surfaces up to high Reynolds numbers. *J. Fluid Mech.* **795**, 210–240.

STULL, R.B. 1988 *An Introduction to Boundary Layer Meteorology*, vol. 13. Springer Science & Business Media.

TALLURU, K.M., BAIDYA, R., HUTCHINS, N. & MARUSIC, I. 2014 Amplitude modulation of all three velocity components in turbulent boundary layers. *J. Fluid Mech.* **746**, R1.

TAYLOR, G.I. 1938 The spectrum of turbulence. *Proc. R. Soc.* A **164** (919), 476–490.

TIELEMAN, H.W. 2008 Strong wind observations in the atmospheric surface layer. *J. Wind Engng Ind. Aerodyn.* **96** (1), 41–77.

TOWNSEND, A.A. 1976 *The Structure of Turbulent Shear Flow*, 2nd edn. Cambridge University Press.

VALLIKIVI, M., GANAPATHISUBRAMANI, B. & SMITS, A.J. 2015 Spectral scaling in boundary layers and pipes at very high Reynolds numbers. *J. Fluid Mech.* **771**, 303–326.

VAN DER HOVEN, I. 1957 Power spectrum of horizontal wind speed in the frequency range from 0.0007 to 900 cycles per hour. *J. Meteorol.* **14** (2), 160–164.

VICKERS, D. & MAHRT, L. 1997 Quality control and flux sampling problems for tower and aircraft data. *J. Atmos. Ocean. Technol.* **14** (3), 512–526.

VON STORCH, H. & ZWIERS, F.W. 1999 *Statistical Analysis in Climate Research*. Cambridge University Press.

WANG, G. & ZHENG, X. 2016 Very large scale motions in the atmospheric surface layer: a field investigation. *J. Fluid Mech.* **802**, 464–489.

WELCH, P. 1967 The use of fast Fourier transform for the estimation of power spectra: a method based on time averaging over short, modified periodograms. *IEEE Trans. Audio Electroacoust.* **15** (2), 70–73.

WILCZAK, J.M., ONCLEY, S.P. & STAGE, S.A. 2001 Sonic anemometer tilt correction algorithms. *Boundary-Layer Meteorol.* **99** (1), 127–150.

WILSON, J.D. 2008 Monin-Obukhov functions for standard deviations of velocity. *Boundary-Layer Meteorol.* **129** (3), 353–369.

WYNGAARD, J.C. 2004 Toward numerical modeling in the 'terra incognita'. *J. Atmos. Sci.* **61** (14), 1816–1826.

YAMAMOTO, Y. & TSUJI, Y. 2018 Numerical evidence of logarithmic regions in channel flow at $Re_\tau = 8000$. *Phys. Rev. Fluids* **3** (1), 012602.

YANG, X.I.A. & MENEVEAU, C. 2019 Hierarchical random additive model for wall-bounded flows at high Reynolds numbers. *Fluid Dyn. Res.* **51** (1), 011405.

ZHAN, L., LETIZIA, S. & IUNGO, G.V. 2020 Lidar measurements for an onshore wind farm: wake variability for different incoming wind speeds and atmospheric stability regimes. *Wind Energy* **23** (3), 501–527.